nagra National Cooperative for the Disposal of Radioactive Waste

TECHNICAL REPORT 92-14

Mechanical Behaviour of High Level Nuclear Waste Overpacks under Repository Loading and During Welding

March 1994

R. Attinger
G. Duijvestijn

PSI, Würenlingen and Villigen

Hardstrasse 73, CH-5430 Wettingen/Switzerland, Telephone +41-56-37 11 11

nagra National Cooperative for the Disposal of Radioactive Waste

TECHNICAL REPORT 92-14

Mechanical Behaviour of High Level Nuclear Waste Overpacks under Repository Loading and During Welding

March 1994

R. Attinger
G. Duijvestijn

PSI, Würenlingen and Villigen

Hardstrasse 73, CH-5430 Wettingen/Switzerland, Telephone +41-56-37 11 11

This report was prepared as an account of work sponsored by Nagra. The viewpoints presented and conclusions reached are those of the author(s) and do not necessarily represent those of Nagra.

SUMMARY

One of the concepts for final disposal of high level nuclear waste in Switzerland consists of a mined repository approximately 1200 m deep in the crystalline bedrock of Northern Switzerland. In order to delay the return of the radionuclides to the biosphere, and to reduce their concentration there to acceptable levels, reliance is placed in the multiple safety barrier principle. In addition to the natural barriers (host rock and overlying sediments), the following engineered barriers are envisaged: the waste form itself (vitrified high level nuclear waste), an overpack, the purpose of which is to ensure isolation of the radionuclides from groundwater for a period of at least 1000 years, and a compacted bentonite backfill within which the overpack is placed horizontally in the axis of the repository gallery. This backfill is aimed at reducing the transport of water and dissolved species from the waste to the host rock.

The first part of the present work reports on the participation in the COMPAS project (COntainer Mechanical Performance ASsessment). This project was carried out within the framework of the European Atomic Energy Community's cost–sharing programme on 'Radioactive Waste Management and Disposal'. It was concerned with the mechanical performance of overpacks for vitrified high level nuclear waste. First, the COMPAS project was intended to demonstrate that overpacks can be designed which will be able to withstand the loadings anticipated in deep geological repositories. Second, it investigated the current analytical capability with regard to the prediction of the behaviour of overpacks under both anticipated repository loads and extreme loading conditions. There has been a strong emphasis on predictive finite element calculations in the COMPAS project, with experimental testwork to provide data to check the calculations, through a series of models ranging from simple rings to realistic scale models, one in the form of the overpack from NAGRA. One of our aims in the COMPAS project was to verify the finite element code used with experiments which are relevant to the design of overpacks.

The second part of this work deals with the issue of stress corrosion cracking of the high level nuclear waste overpack from NAGRA which is made out of GS-40 cast steel. The design work carried out for the overpack (STEAG & MOTOR–COLUMBUS 1984) showed for the stresses a safety margin of a factor 5 against the tensile strength. The issue of stress corrosion cracking must be raised whenever large tensile stresses are expected, even when a low strength steel with potentially good resistance to this type of corrosion is used. A project was initiated by NAGRA in order to deal with this issue, the aims being to assess

1) the stress corrosion behaviour of the reference steel in a more detailed manner than in the earlier projects and including laboratory testing,

2) the possibilities for modelling welding stresses and their full or partial relief using 'state–of–the–art' computer codes and

3) the feasibility of achieving adequate relief of the welding stresses.

The above–mentioned aim (2) is the subject of the second part of this work. After a description of the material properties of GS-40 cast steel, the one–dimensional FIBRE model is discussed, which should give an insight into the parameters involved in a thermomechanical calculation of a welding process. Next the thermomechanical calculation for the evaluation of residual stresses using the finite element method is described; it includes the calculation procedure and the verification of the proposed user–supplied material model for the simulation of the material behaviour at high temperature and during multipass welding and stress relief.

The calculations were performed with the commercially available finite element code ADINA (ADINA 1984). The output from ADINA was used as input to the post–processor ORVIRT (BASS & BRYSON 1983) when fracture calculations are considered. During the simulation of the welding process, the need for a user–supplied material model for the simulation of material behaviour at high temperature became obvious. This was implemented in the finite element code SOLVIA (SOLVIA 1987) which was derived from ADINA version 84.

The work presented allows to conclude the following:

- The commercially available finite element code ADINA is suitable for the stress analysis of high level nuclear waste overpacks under repository loading and during welding.

- It was demonstrated that the behaviour of an overpack can be modelled to a level of accuracy within engineering limits with the help of the finite element code ADINA. The verification and validation work performed in the COMPAS project treated creep, fracture mechanics problems and buckling; the experiments were simulated by two–dimensional or three–dimensional models considering elasto–plastic material behaviour and large displacements. The material model used to simulate the material behaviour at high temperature was verifyed with an experiment where two annuli are welded together by means of electro–beam welding.

- The assumptions used in the thermomechanical calculations for the simulation of the welding process are important for the residual shape of the workpiece, but not for the residual stresses. The calculated residual stresses are high and, therefore, they are limited by the yield limit. The calculated tensile stresses around the weld may reach the yield limit.

- The stress relief obtained in a post–weld heat treatment may be maintained during the subsequent cooling to ambient temperature when the cooling process is performed appropriately. Rapid cooling may result in large residual stresses which will not be reduced in all cases, even if viscous effects are considered.

ZUSAMMENFASSUNG

In der Schweiz sieht eines der Entsorgungskonzepte für hochradioaktive Abfälle vor, ein Endlager in einer Tiefe von etwa 1200 m im kristallinen Grundgestein der Nordschweiz zu errichten. Bei diesem Konzept wurde Wert auf das Prinzip mehrfacher Sicherheitsbarrieren gelegt, um in ihnen die Rückkehr der Radionuklide zur Biosphäre zu verzögern und dabei ihre Konzentration auf annehmbare Werte zu reduzieren. Neben den natürlichen Barrieren (Wirtgestein und überlagerte Sedimente) sind folgende ingenieurmässigen Barrieren vorgesehen: Die Form des verglasten hochradioaktiven Abfalls selber und ein mit verdichtetem Bentonit hinterfüllter, horizontal in der Achse des Endlagers angeordneter Endlagerbehälter. Der Endlagerbehälter soll während mindestens 1000 Jahren dicht bleiben und die Radionuklide vom Grundwasser isolieren. Die Hinterfüllung aus Bentonit soll den Transport von Wasser und gelösten Partikeln zwischen dem hochradioaktiven Abfall und dem Wirtgestein reduzieren.

Der erste Teil der vorliegenden Arbeit berichtet über die Teilnahme am Projekt COMPAS (COntainer Mechanical Performance ASsessment). Dieses Projekt wurde im Zusammenhang mit dem Atomenergieprogramm 'Radioactive Waste Management and Disposal' der Europäischen Gemeinschaft ausgeführt und konzentriert sich auf das mechanische Verhalten von Endlagerbehältern für hochradioaktiven Abfall. Das Projekt COMPAS verfolgte zwei Ziele. Erstens sollte nachgewiesen werden, dass Endlagerbehälter entworfen werden können, welche den geologischen Belastungen tiefliegender Endlager standhalten. Und zweitens sollten die analytischen Möglichkeiten herausgefunden werden, mit denen das Verhalten von Endlagerbehältern sowohl unter den geologischen Belastungen tiefliegender Endlager als auch unter Belastungen infolge von extremen Bedingungen vorhergesagt werden kann. Im Projekt COMPAS wurde grosses Gewicht auf vorhersagende Berechnungen gelegt. Daher wurden mit Experimenten an Modellen, ausgehend von einfachen Ringmodellen bis zu realen, massstäblichen Modellen beispielsweise in Form des Endlagerbehälters der NAGRA, die erforderlichen Daten für eine Überprüfung der Berechnungen bereitgestellt. Unser Interesse an einer Teilnahme am Projekt COMPAS bestand darin, das verwendete Finite Elemente Programm an Experimenten zu verifizieren, die für den Entwurf von Endlagerbehältern relevante Probleme behandeln.

Der zweite Teil dieser Arbeit befasst sich mit dem Themenkreis Spannungsrisskorrosion beim Endlagerbehälter der NAGRA für die Endlagerung verglaster hochradioaktiver Abfälle. Die durchgeführten Berechnungen (STEAG & MOTOR–COLUMBUS 1984) zur Dimensionierung des Endlagerbehälters aus Stahlguss GS-40 weisen für die Spannungen einen Sicherheitsfaktor von 5 gegenüber der Zugfestigkeit nach. Fragen betreffend Spannungsrisskorrosion müssen nun aber dann gestellt werden, wenn grosse Zugspannungen erwartet werden, auch wenn niedrigfester Stahl mit seinem potentiell guten Widerstand gegenüber dieser Art von Korrosion eingesetzt wird. Bei der NAGRA wurde ein Projekt zu diesem Themenkreis mit folgenden Zielen iniziiert:

1) das Verhalten des Referenzstahls auf Spannungsrisskorrosion detaillierter als in den früheren Projekten zu untersuchen und Laboruntersuchungen einzubeziehen,

2) die Möglichkeiten von Computerprogrammen bei der Ermittlung von Schweisseigenspannungen sowie deren vollen oder teilweisen Abbau abzuklären sowie

3) die Eignung verschiedener Methoden für einen ausreichenden Abbau der Schweisseigenspannungen festzulegen.

Der oben erwähnte Punkt (2) ist Gegenstand des zweiten Teils dieser Arbeit. Nach einer Beschreibung der Materialeigenschaften von Stahlguss GS-40 wird das eindimensionale Modell FIBRE diskutiert, welches Einblick in die bei thermomechanischen Berechnungen von Schweissprozessen involvierten Parameter geben soll. Dann werden die thermomechanischen Berechnungen zur Bestimmung der Schweisseigenspannungen mit der Methode der Finiten Elemente beschrieben: Es werden der Berechnungsablauf, die Verifikation des vorgeschlagenen Materialmodells zur Simulation des Materialverhaltens bei hohen Temperaturen, Mehrlagenschweissung und Abbau von Schweisseigenspannungen dargelegt.

Die Berechnungen wurden mit dem kommerziellen Finite Elemente Programm ADINA (ADINA 1984) durchgeführt. Die Resultate von ADINA wurden als Eingabe für den Postprozessor ORVIRT (BASS & BRYSON 1983) verwendet, wenn Bruchmechanikprobleme zu behandeln waren. Während den Arbeiten zur Simulation des Schweissprozesses wurde offensichtlich, dass zur Beschreibung des Materialverhaltens bei hohen Temperaturen ein eigenes Materialmodell erforderlich ist. Dieses Materialmodell wurde im Finite Elemente Programm SOLVIA (SOLVIA 1987) eingebaut; SOLVIA wurde aus der Version 84 des Programms ADINA abgeleitet.

Die vorliegende Arbeit lässt folgende Folgerungen zu:

- Das kommerzielle Finite Element Programm ADINA eignet sich, Spannungsanalysen an den Endlagerbehältern zur Lagerung hochradioaktiver Abfälle unter den geologischen Belastungen tiefliegender Endlager wie auch während des Schweissens durchzuführen.

- Es wurde gezeigt, dass mit dem Finite Elemente Programm ADINA das Verhalten von Endlagerbehältern mit einem Genauigkeitsgrad bestimmt werden kann, der innerhalb von realistischen, ingenieurmässigen Grenzwerten liegt. Die innerhalb des Projekts COMPAS ausgeführten Validierungs– und Verifizierungsarbeiten behandelten Kriechvorgänge, Bruchmechanikprobleme und Beulen. Die Experimente wurden mit zwei– und dreidimensionalen Modellen simuliert, in denen elasto–plastisches Materialverhalten vorausgesetzt und grosse Verschiebungen berücksichtigt wurden. Das Materialmodell zur Simulation des Materialverhaltens bei hoher Temperatur wurde an Hand eines Experiments verifiziert, wo zwei Ringe mittels Elektrostrahlschweissen zusammengefügt wurden.

- Die in die thermomechanischen Berechnungen eingehenden Annahmen für die Simulation des Schweissprozesses sind wichtig für die Form des Werkstücks, nicht jedoch für die Eigenspannungen, da die berechneten Eigenspannungen hoch sind und dadurch von der Fliessgrenze begrenzt werden. Die berechneten Zugspannungen um die Schweissnaht herum können die Fliessgrenze erreichen.

- Der in einer Wärmebehandlung nach dem Schweissen erzielte Spannungsabbau kann in der daran anschliessenden Abkühlung auf Raumtemperatur erhalten bleiben, wenn die Abkühlung in geeigneter Weise erfolgt. Rasches Abkühlen kann hohe Eigenspannungen erzeugen, welche auch bei Berücksichtigung viskoser Effekte nicht unbedingt kleiner ausfallen werden.

RESUME

Un des concepts pour l'entreposage définitif des déchets hautement radioactifs en Suisse consiste en un dépôt à une profondeur d'environ 1200 m dans le socle granitique de la Suisse septentrionale. On tient beaucoup dans ce concept aux barrières multiples qui doivent retarder le retour des radionuclides vers la biosphère et ainsi réduire leur concentration à un niveau acceptable dans la biosphère. En plus des barrières naturelles (rocher d'hôte et couches de sédiments superposées), les barrières artificielles suivantes ont été prévues: la forme vitrifiée des déchets hautements radioactifs eux-mêmes et un conteneur placé horizontalement dans l'axe du dépôt. Le conteneur est entouré de bentonite comprimée. Le conteneur doit rester étanche pendant au moins 1000 ans et isoler les radionuclides des eaux souterraines. Le remplissage en bentonite doit réduire le transport de l'eau et des particules dissoutes entre les déchets et le rocher d'hôte.

La première partie du travail présenté porte sur la participation au projet COMPAS (COntainer Mechanical Performance ASsessment). Ce projet a été exécuté en relation avec le Programme d'Energie Atomique 'Radioactive Waste Management and Disposal' de la Communauté Européenne; il se concentre sur le comportement mécanique des conteneurs d'entreposage pour les déchets hautement radioactifs. Le projet COMPAS poursuit deux buts. Le premier est de prouver que l'on peut concevoir un conteneur capable de résister aux charges géologiques dans un dépôt en grande profondeur. Le deuxième est de trouver une méthode analytique permettant de prédire le comportement des conteneurs non seulement sous cette charge géologique mais aussi sous une charge correspondant à des conditions extrêmes. Dans le projet COMPAS, un grand poids a été donné aux calculs de prédiction. Dans ce sens, les données nécessaires à un contrôle des calculs ont été préparées. Ces données ont été établies sur la base d'expériences sur modèles allant de modèles simples de forme d'anneaux jusqu'à des modèles réels et à l'échelle de forme du conteneur de la CEDRA par exemple. Notre intérêt à une participation au projet COMPAS résidait dans la vérification des programmes d'éléments finis appliqués aux expériences, ces expériences ayant montré des problèmes importants à résoudre pour la conception des conteneurs.

La deuxième partie de ce travail concerne le sujet général de la fissuration par corrosion sous contrainte du conteneur de la CEDRA pour l'entreposage définitif des déchets hautement radioactifs vitrifiés. Les calculs réalisés (STEAG & MOTOR–COLUMBUS 1984) pour le dimensionnement du conteneur fabriqué à partir d'acier coulé GS-40

montrent pour les contraintes un facteur de sécurité de 5 par rapport à la limite élastique en tension. Des questions concernant la fissuration par corrosion sous contrainte doivent cependant toujours être posées si l'on s'attend à de grandes contraintes en tension, même s'il s'agit d'un acier à basse limite élastique avec une bonne résistance potentielle contre ce type de corrosion. A la CEDRA, un projet a été initié sur ce thème avec les buts suivants:

1) étude du comportement de l'acier de référence à la fissuration par corrosion sous contrainte plus détaillée que dans les projets précédents et utilisation des examens de laboratoires,

2) possibilité d'application de programmes pour la détermination des contraintes résiduelles de soudure et possibilité de l'élimination ou réduction de ces contraintes, et

3) possibilité d'établir l'aptitude de différentes techniques pour une réduction suffisante des contraintes résiduelles de soudure.

Le point (2) est l'objet de la deuxième partie de ce travail. Après une description des proriétés de l'acier coulé GS-40, le modèle unidimensionnel FIBRE sera discuté. Ce modèle devrait donner un aperçu sur les paramètres impliqués dans les calculs thermomécaniques des procédés de soudage. Les calculs thermomécaniques pour la détermination des contraintes résiduelles de soudure avec la méthode des éléments finis seront alors décrites. On présentera le déroulement des calculs, la vérification des modèles proposés pour le matériau pour ses propriétés aux hautes températures, le soudage par couches multiples et la réduction des contraintes résiduelles de soudure.

Les calculs sont faits avec le programme commercial d'éléments finis ADINA (ADINA 1984). Les résultats d'ADINA ont été utilisés comme données d'entrée au processeur ORVIRT (BASS & BRYSON 1983) pour les calculs de mécanique des fissures. Il est apparu clairement pendant les travaux de simulation de soudage que la description du comportement du matériau à hautes températures nécéssitait un propre modèle. Ce modèle a été introduit dans le programme d'éléments finis SOLVIA (SOLVIA 1987). SOLVIA a été déduit de la version 84 du programme ADINA.

Le travail présenté permet de tirer les conclusions suivantes:

- Le programme commercial d'éléments finis ADINA est approprié pour faire les analyses de contraintes pour les conteneurs de déchets hautement radioactifs pour leur entreposage définitif en grande profondeur ainsi que pour le soudage.

- Il a été montré avec le programme d'éléments finis ADINA que le comportement des conteneurs peut être simulé avec un degré de précision au dedans des valeurs limites réalistes d'ingénieur. Les travaux de validation et de vérification réalisés dans le projet COMPAS incluent le fluage transitoire, les problèmes de mécanique des fissures et les flambages. Les expériences ont été simulées avec des modèles à deux et trois dimensions pour lesquels un comportement élasto-plastique du matériau a été supposé et les grands déplacements considérés. Le modèle pour

simuler le comportement du matériau à hautes températures a été vérifié par l'expérience des deux anneaux soudés électriquement.

- Les hypothèses introduites dans les calculs thermomécaniques pour la simulation du soudage sont importantes pour la forme de la pièce; elles ne le sont pas pour les contraintes résiduelles parce que ces contraintes sont grandes mais en dessous de la limite élastique. Les contraintes de tension autour de la soudure peuvent atteindre la limite élastique.

- La réduction des contraintes par chauffage après le soudage peut être conservée après le refroidissement à la température ambiante si ce refroidissement est fait de manière appropriée. Un refroidissement rapide peut produire des contraintes résiduelles élevées, qui même en considérant les effets de viscosité, ne seront pas obligatoirement réduites.

Contents

1 High level nuclear waste overpacks under extreme geological loading conditions: the work performed within the COMPAS project

1.1 Introduction to the COMPAS project

The COMPAS project was a European project, with the participation of partners from six European countries (Table 1). It was concerned with the mechanical performance of overpacks for vitrified high level nuclear waste (OVE ARUP & PARTNERS 1989 and 1990).

Two alternative overpack concepts were identified at the outset of the COMPAS project. One, a thin–walled concept, relied on a thin corrosion resistant wall for the overpack (titanium alloy) which was supported by a filler (lead or particulate material), with the loads being transmitted to the high level nuclear waste. The other, a thick–walled concept, uses a material such as mild steel to provide a stressed overpack, with sufficient thickness to withstand the loading in the repository and to allow for corrosion of the overpack.

Two benchmark exercises on both types of overpack were chosen to start the COMPAS project. From these exercises it was decided that most of the efforts in the COMPAS project would be directed to a study of the thick–walled overpack concept. The test programme for the COMPAS project splits into three categories:

1) A series of preliminary tests, involving very simple geometries and loading conditions, aimed at checking the performance of the computer codes and analytical techniques for material and geometrical non–linearities.
2) A series of intermediate tests, involving simplified scale models of overpacks under extreme pressure conditions to see the effect of geometrical variations.
3) A series of advanced tests, involving scale models of typical overpacks.

Calculations and testing have focused on the behaviour of the overpacks under both anticipated repository loads and extreme loading conditions up to the point of collapse. However, the testwork, of necessity, looks only at hydrostatic pressures on the overpacks. The loading is unlikely to be hydrostatic in real repositories and typically will have a large hydrostatic component, some pinch loading and possibly some point loading. It is because of the complexity of the real repository loading that so much emphasis has been placed on finite element modelling in the COMPAS project.

The calculations were carried out in parallel with the experiments and the results of the calculations were compared with those of the experiments. For the finite element calculations, material and geometrical data, along

Table 1: Partners in the COMPAS project and the finite element codes used (OAP 1989a).

Partner	Finite element code	Computer
Ove Arup & Partners [1] Great Britain	DYNA3D, NIKE2D, PAFEC	VAX 11/785
	DYNA3D	CONVEX C210 [3]
SCK–CEN Belgium	CASTOR BE-2D	HP9000 Series 310
	SYSTUS	μVAX, IBM 4381
CEA France	CASTEM – INCA	CRAY I
STEAG Kernenergie GmbH Germany	COSMOS/M	IBM PC AT03
Equipos Nucleares SA [2] Spain	ANSYS	HP9000 Series 310, HP9000 Series 320
PSI/NAGRA Switzerland	ADINA	APOLLO DN3000, APOLLO DN4000,
	ADINA/SOLVIA	CRAY X–MP/28 [3]

[1]: OAP was responsible for experiments and comparison of the results.
[2]: ENSA manufactured the tested overpacks.
[3]: Computers used for the advanced testwork.

with details of loading, were supplied to all the partners, but choice of finite element code and details of the finite element modelling were left to the partners. Different computer codes were used to analyse these problems (Table 1) on a range of machines from PCs through mini–computers to super computers.

All the specimens for one experiment were machined from the same piece of mild steel. Tensile tests were performed on samples from the same steel; each test was repeated three times and the results were found to be consistent. The resulting load vs. displacement curves were made available to the partners in graphical form but were not processed by the project coordinator OAP (Ove Arup & Partners, Great Britain); a summary of typical strength parameters is given in Table 2. Different codes use different material models and each partner was free to process the results of the tensile tests with their own code requirements in mind.

Table 2: Typical strength parameters of the mild steels used in the COMPAS project.

Testwork	Sample from	Yield limit $Rp_{0.2}$ [MPa]	Ultimate strength Rm [MPa]
Preliminary ring test	Bar	237	506
Intermediate testwork	Bar	277	545
	Plate	271	449
Advanced testwork	Bar	261	506

1.2 Benchmark exercises

Two benchmark exercises on both types of overpack were selected (OAP 1989b). One looked at the long–term response of part of a thin–walled overpack with lead filler to an external pressure and the other looked at the response of a slice through a thick–walled overpack under pressure. These benchmark exercises were used to evaluate the capabilities of various computer codes for these types of stress calculations.

1.2.1 Thin–walled overpack

It was originally intended to show the creep calculation capabilities of the codes in this benchmark exercise. However, as only two results were presented, a comparison concerning creep was seen to be of limited value. Thus, the comparisons have been made on the basis of elastic calculations (Table 3). The predicted stress levels were in reasonably good agreement. The base end of the overpack, the titanium overpack wall (Fig. 1.1), was stiffer than the lead filler because of its doubly curved shape. Consequently, a greater proportion of the load was carried by the titanium overpack wall.

Table 3: Effective stresses [MPa] in the thin–walled overpack based on an elastic two–dimensional calculation due to an external pressure of 40 MPa.

Partner	Code	Titanium	Lead	Waste
OAP	NIKE	17 ÷ 35	0.3 ÷ 6	0.2 ÷ 6
SCK–CEN	CASTOR BE-2D	15 ÷ 36	3 ÷ 10	0 ÷ 3
CEA	CASTEM – INCA	–	2 ÷ 6	1 ÷ 5
STEAG	COSMOS/M 2D	15 ÷ 37	4 ÷ 15	0 ÷ 4
	COSMOS/M 3D	12 ÷ 34	5 ÷ 21	2 ÷ 6
PSI/NAGRA	ADINA	17 ÷ 36	0.2 ÷ 7.3	0.3 ÷ 6

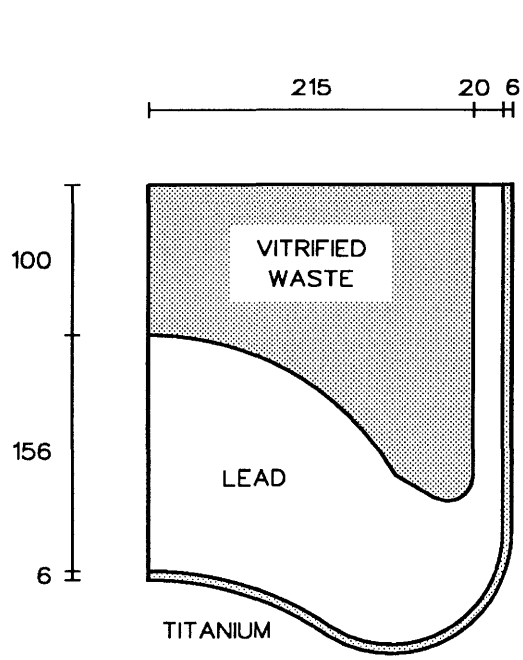

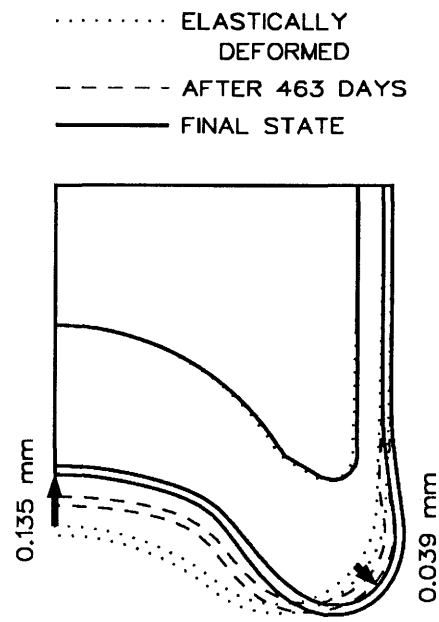

Fig. 1.1a: Bottom part of the thin–walled overpack (all dimensions are in mm).

Fig. 1.1b: Evolution of the deformation of the thin–walled overpack under an external pressure of 40 MPa when the lead is allowed to creep.

In the next stage, the lead filler was allowed to creep according to a creep law in which only secondary creep was considered, whereas the titanium overpack and the waste continued to behave elastically. Only OAP and PSI/NAGRA carried out a conventional creep calculation in which the transient behaviour of the overpack from an initial elastic state to a creep state over a period of around 400 days was studied. Both of these calculations were in two dimensions and the evolution of the displacements showed quite close agreement.

One of the features of the creep behaviour was the redistribution of stresses from an initial elastic state to a stationary or final stress distribution. In an effort to identify the time required for the overpack to reach the final creep state, OAP extended the transient creep calculation to 1000 years, a typical design lifetime for high level nuclear waste overpacks. At this time, the deviatoric stress component still continues to decrease but at a much reduced rate. A comparison with the final state (as determined in the next paragraph) reveals that the overpack is far from reaching the final creep state, e.g. the axial displacement at the bottom after 1000 years is about 42 % of the final state deformation.

CEA carried out a useful alternative to the conventional transient creep calculation to determine the final creep state. The lead filler is reduced to a hydrostatic state of stress because of its inability to sustain shear stress due to creep. The lead behaves like a fluid at the limit; thus it is treated as a

fluid that has no shear strength in the final creep state calculation. Figure 1.1 depicts the deformed shape of the overpack at different times as calculated by PSI/NAGRA.

OAP investigated further non–linearity in the form of sliding motion at the interfaces between the titanium overpack and the lead filler and between the lead filler and the block of high level nuclear waste. In the case of frictionless interfaces, sliding motion is quite noticeable between the lead filler and the titanium overpack at the corner region. On the other hand, sliding motion is almost negligible at the interfaces after a period of 50 years when a small friction coefficient is considered and, therefore, a long–term transient creep calculation would resemble the one where the interfaces are perfectly bonded.

1.2.2 Thick–walled overpack with uniformly corroded profile

This test was chosen in order to show the elasto–plastic calculation capabilities of the finite element codes. It was required to predict the external pressure which causes a reduction of 10 mm in the internal diameter (440 mm) of a 60 mm thick overpack. The 10 mm correspond to the overpack collapsing onto the canister with high level nuclear waste.

Table 4: Pressure for 10 mm of reduction in the internal diameter of the uniformly corroded overpack.

Partner	Code	Calculation [1)]	Pressure [MPa]
OAP	DYNA3D	three–dimensional	80.5
SCK–CEN	CASTOR BE-2D	only elastic	–
CEA	CASTEM – INCA	small displacement	81.6
		large displacement	112.5
STEAG	COSMOS/M	standard	78.4
ENSA	ANSYS	standard	82.3
PSI/NAGRA	ADINA	two–dimensional	77.7

1): An elasto–plastic two–dimensional calculation in a small displacement formulation was used as a standard.

There is a good correlation in the elastic range, although there is a degree of divergence in the plastic range. The variation in the stresses could have been due to different modelling strategies used by the partners (axisymmetric, two–dimensional plane strain or three–dimensional), different mesh patterns across the thickness, different number of Gaussian integration points (ranging from 3*3 to 1*1*1) or different techniques used by the codes for calculating the stresses at the nodal points from the stresses at the Gaus-

sian integration points. Nevertheless, predictions of the pressure required to reduce the internal diameter by 10 mm fall within a range that is roughly ±2.5 % about the mean (Table 4) when a small displacement formulation is used. This is considered to be quite good for this class of problem for which no simple closed–form solution exists. A large displacement formulation seems to stiffen the overpack.

1.2.3 Thick–walled overpack with non–uniformly corroded profile

The second stage exchanged the uniformly corroded profile for a non–uniform one. Again, the elasto–plastic calculation was to predict the pressure required to achieve a 10 mm reduction in the internal diameter of the overpack.

The pressure–displacement curves are in general agreement in the initial elastic phase but begin to deviate in the plastic phase where all the curves, except for the CEA large–displacement formulation, show continuing hardening behaviour. The predicted critical pressures that causes the required reduction are given in Table 5.

Table 5: Pressure for 10 mm of reduction in the internal diameter of the non–uniformly corroded overpack.

Partner	Code	Calculation [1]	Pressure [MPa]
OAP	DYNA3D	three–dimensional	61
SCK–CEN	CASTOR BE-2D	only elastic	–
CEA	CASTEM – INCA	small displacement	– [2]
		large displacement	– [2]
STEAG	COSMOS/M	only elastic	–
ENSA	ANSYS	standard	68
PSI/NAGRA	ADINA	two–dimensional	67
		three–dimensional	– [2]

[1]: A two–dimensional calculation in a small displacement formulation was used as a standard.

[2]: Calculation stopped before the required reduction was reached.

1.2.4 Thick–walled overpack with uniformly corroded and cracked profile

This problem was to determine the pressure which leads to the unstable growth of a crack situated at the root of a 5 mm notch in the uniformly corroded overpack under sinusoidal pressure (with its maximum at the notch).

Table 6: Critical pressure for growth of a 5 mm long crack in the uniformly corroded overpack.

Partner	Code	Calculation [1)]	Pressure [MPa]
OAP	PAFEC	two–dimensional	21.2
		three–dimensional	21.2
CEA	CASTEM – INCA	standard	20.3
STEAG	COSMOS/M	no crack calculation	–
ENSA	ANSYS	three–dimensional	21.6
PSI/NAGRA	ADINA	elastic	20.0
		elasto–plastic	18.3

[1)]: A two–dimensional elastic calculation in a small displacement formulation was used as a standard.

The critical pressure was defined as that which caused the stress intensity factor K_I to reach the critical value K_{IC}.

This test was chosen to compare the crack/fracture calculation capabilities of the codes. The predicted critical pressures are listed in Table 6. The PSI/NAGRA result shows that plasticity near the crack tip region reduces the pressure required for unstable crack growth. It is interesting to note that their effective stress and effective plastic strain countours for the elasto–plastic calculation confirm that plastic deformation is confined locally to the crack tip region. This suggests that plasticity is a factor that needs careful consideration in future fracture calculations.

1.3 Preliminary ring tests

The preliminary ring tests were intended as a series of tests which could be easily defined and would not require expensive test facilities (OAP 1989c). As a result, four variations on a simple ring under transverse loading were tested. The first (R1) is a simple uncracked ring, the second (R2) and third (R3) are rings with external and internal cracks respectively, and the fourth (R4) is a ring which has weld material deposited on the outside, leaving a ring consisting of two materials and a heat affected zone. All the rings were machined from the same piece of a mild steel bar. The geometry of the rings (outer diameter 160 mm, inner diameter 128 mm, crack depth 8 mm) was chosen to be representative of a section through a thick–walled overpack. However, the loading is somewhat artificial in that the ring is squeezed between two flat plattens of the loading device.

This problem involved large deformations, large strains and cracking, as well as interfaces with moving contact points. The results for the cross–head

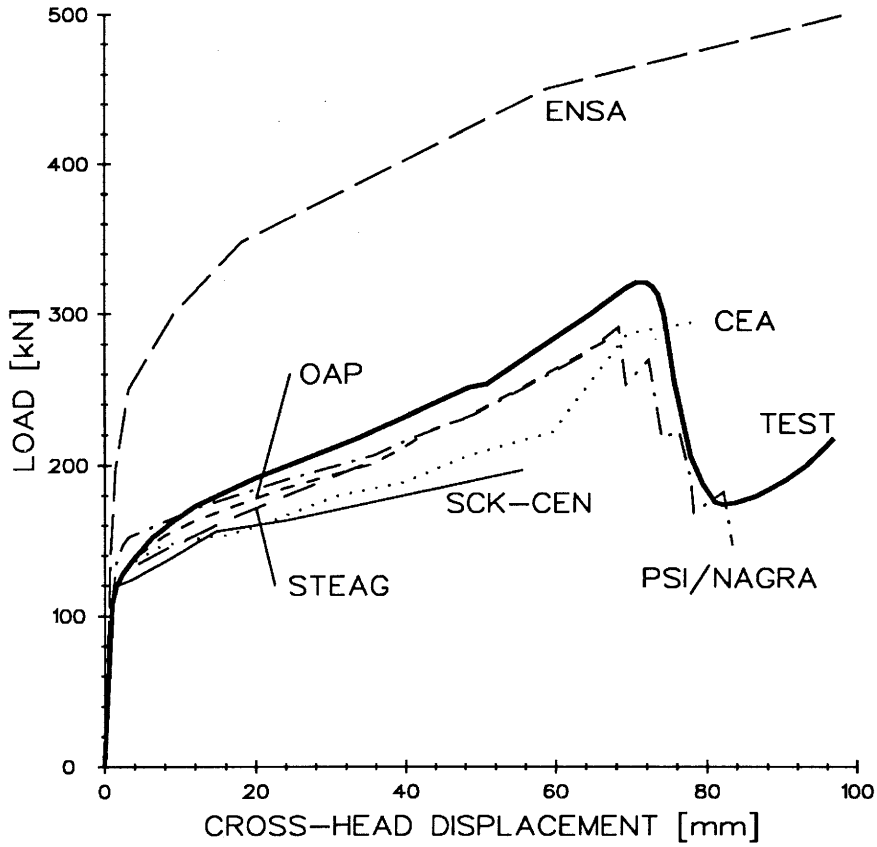

Fig. 1.2: Cross–head displacement of the uncracked ring R1.

displacement for the uncracked ring R1 are shown in Figure 1.2 along with the test curve (which is the average of the three results of the experimental tests). With the exception of one curve, the analytical results show good agreement with the experimental results.

For ring type R1 only, PSI/NAGRA performed their calculation with a user–supplied material law to allow for stress loss at ultimate strength, a measure which is useful for the investigation of the post-failure behaviour but not for predictive calculations where the first reaching of the ultimate strength suffices. The central part in the axial direction of the rings is approximately in a state of plane strain and the outer parts in plane stress. PSI/NAGRA demonstrated that plane strain calculations were superior to plane stress, and that three–dimensional calculations gave even better answers. A large displacement formulation should be considered for strains exceeding about 5 %.

Although the two cracked ring types R2 and R3 behaved differently under load, similar lessons can be learnt from the attempts to model them. The prediction of the load versus cross–head displacement curve is generally good (Fig. 1.3), while the prediction of the load versus crack mouth opening displacement (CMOD) curves is significantly inferior (Fig. 1.3). The latter

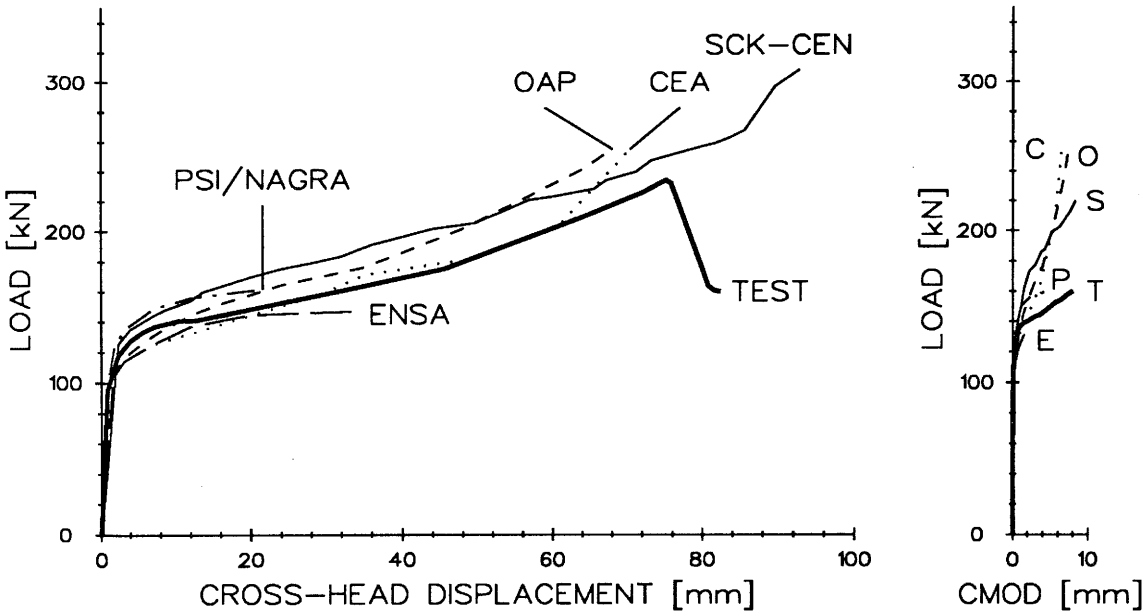

Fig. 1.3: Cross–head displacement and crack mouth opening displacement of the outside cracked ring R2.

indicates that the CMOD curve flattens out at about 1 mm and this is due to the growth of the crack into the ring. Only PSI/NAGRA allowed for crack growth in their calculation; the other partners assumed that the effects of fracture are less significant than the effects of plasticity. Crack length increase was not modelled in the finite element calculation of PSI/NAGRA, but a series of calculations was performed with different crack lengths, and the results were combined with J–Integral calculations to predict the crack behaviour and the load versus displacement curves. The J–Integrals were determined with the post–processor ORVIRT (BASS & BRYSON 1983). ORVIRT is based on the virtual crack extension method. It originated at the Oak Ridge National Laboratory and was further developed at PSI.

Ring type R4 was geometrically identical to ring type R1, but the outer 4 mm of the ring was weld deposit which generally has a greater tensile strength but reduced ductility. The three tests on ring type R4 did not give identical results (Table 7). Ring type R4 was not modelled.

Table 7: Experimental results for ring type R4 with weld deposits.

Number	Peak load [kN]	Failure
R4.1	372	Weld in tension
R4.2	329	Non–welded tension zone on the inside
R4.3	341	Cracks on both the external and internal surfaces

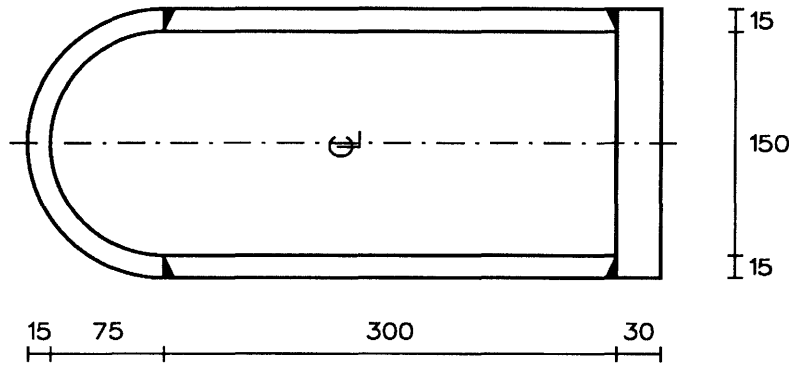

Fig. 1.4a: Standard overpack I1 used in the intermediate testwork.

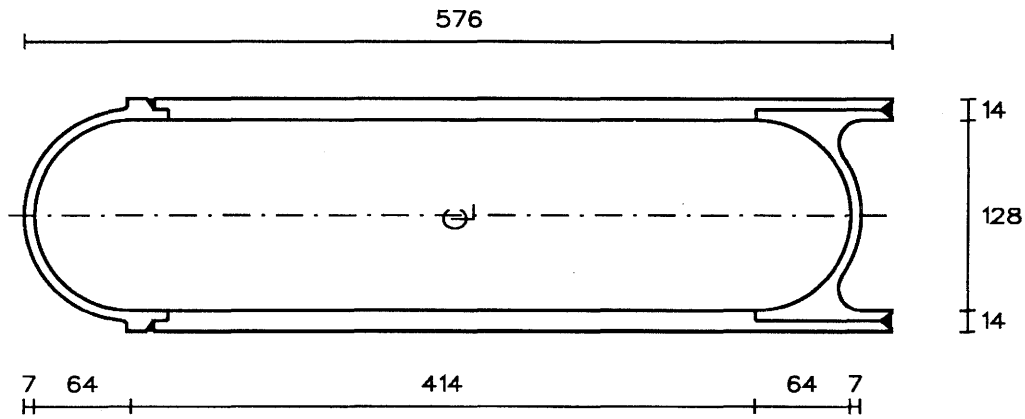

Fig. 1.4b: Overpack A1 with reduced wall thickness used in the advanced testwork.

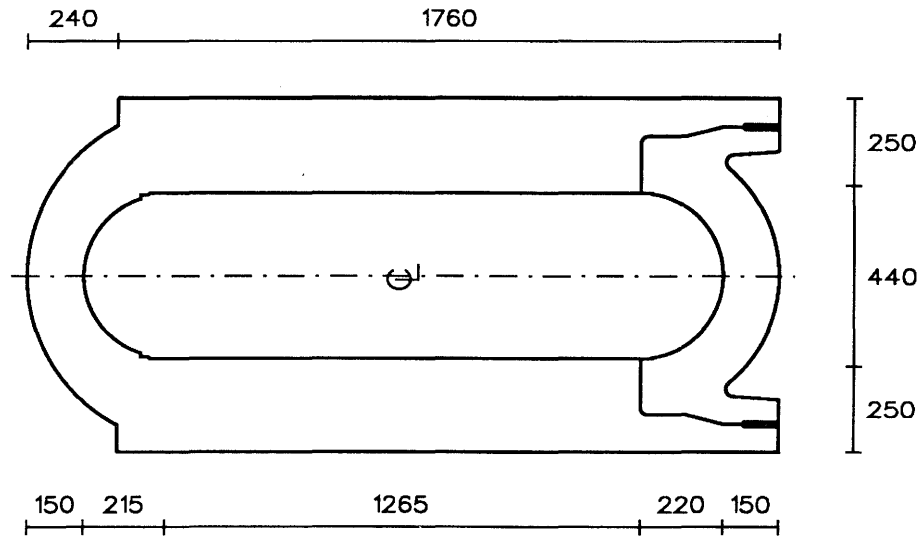

Fig. 1.4c: NAGRA reference overpack.
All dimensions are in mm.

1.4 Intermediate tests on simplified scale models

These tests formed the bulk of the testwork in the COMPAS project (OAP 1990a). A simplified overpack design was produced as shown in Figure 1.4a. This became the reference overpack and variations on this overpack were produced to look at the effect of wall thickness, non–uniform wall thickness, corroded walls and the effect of weld types. The tubular body of each overpack was machined from the same steel bar and the two ends of the overpacks from the same steel plate.

For the standard overpack, three models were made and tested. For each of the other overpacks only one was made and tested. However, the experience with the standard overpack was that the repeatability of the tests was good. Each overpack was tested in a pressure chamber capable of pressures up to 100 MPa. In all tests the temperature was controlled at 20 °C.

Table 8: Failure prediction for the intermediate testwork on simplified overpacks.

Overpack	I1	I2	I3
Description	Standard	Reduced wall thickness	Non–uniform wall thickness
Wall thickness [mm]	15.0	9.0	15.0 ÷ 7.5
Experimental data			
Failure pressure [MPa]	87	35	42
Buckling mode [lobes]	3	3	2
OAP			
Failure pressure [MPa]	91	43	45
Buckling mode [lobes]	4	4	2
SCK–CEN			
Failure pressure [MPa]	>100	52	–
Tensile failure	–	Body	–
CEA			
Failure pressure [MPa]	63	35	34
Buckling mode [lobes]	3	3	2
ENSA			
Failure pressure [MPa]	74	55	–
Tensile failure	Body	Base	–
PSI/NAGRA			
Failure pressure [MPa]	100	44	46
Failure	Plastic hinge	Plastic hinge	2 lobes
Location at interface	Base/Body	Base/Body	Base/Body

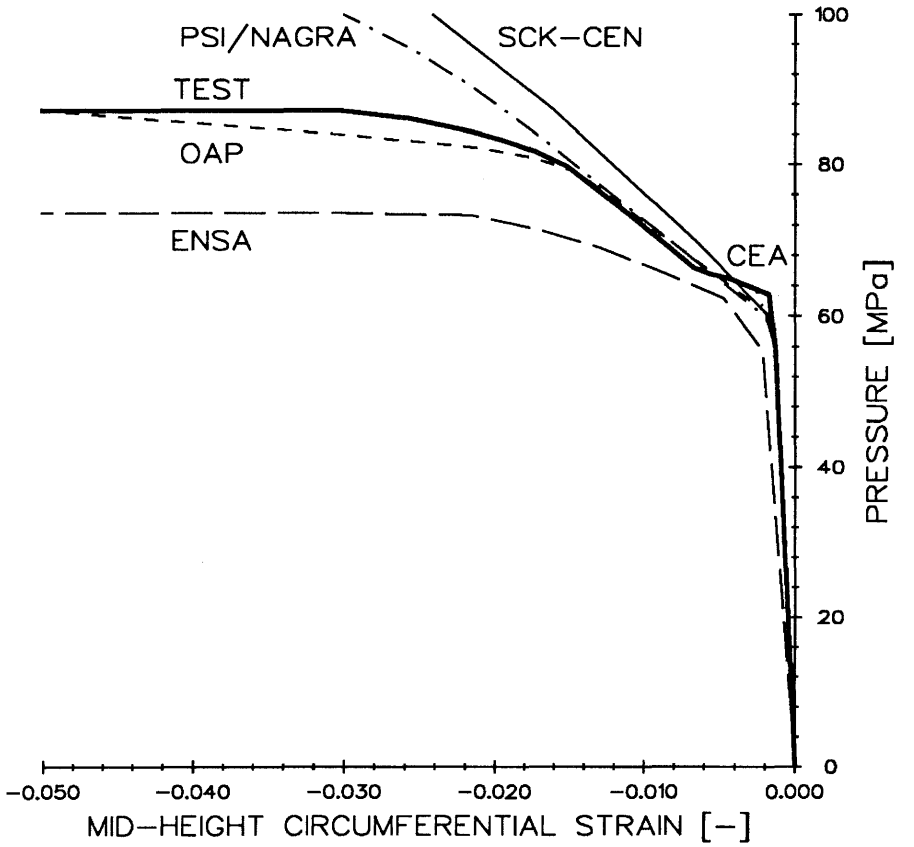

Fig. 1.5: Circumferential strain at mid–height for the standard overpack I1 in the intermediate testwork.

There are two aspects to the calculations for the intermediate tests. Firstly there is the requirement to predict the collapse pressure of the overpacks and secondly to predict the behaviour of the overpacks up to collapse. One of the difficulties in this problem is that the test models do not collapse symmetrically but in a multi–lobe fashion due to plastic buckling. This difficulty is reflected in the variation in prediction of the collapse pressure as shown in Table 8. Various methods were used to predict plastic buckling of the overpacks, which varied from looking for a sudden increase in the distortional energy dissipation to an iterative buckling analysis with successive plastic and buckling calculations.

The other aspect of the calculations was to predict the behaviour of the overpacks up to collapse and this was assessed by comparing the strains at various points on the overpacks as the pressure was increased. The predictions of the circumferential strain (Fig. 1.5) in general showed quite good agreement with the tests for all the studied overpack types, but the prediction of the axial strain was less good. However, it should be noted that the axial components of strain are an order of magnitude lower than the circumferential components, so that prediction of overall strain levels gives quite good agreement.

Table 9: Observed failure for the intermediate testwork on simplified overpacks.

Overpack	I1	I4	I5
Description	Standard	Standard	Corroded surface
Welding type	TIG	Electro–beam	TIG
Wall thickness [mm]	15.0	15.0	15.0 ÷ 7.5
Experimental data			
Failure pressure [MPa]	87	83	75
Buckling mode [lobes]	3	3	3

Further calculations were carried out by PSI/NAGRA to evaluate the relative effects of different material laws. The variation of the Poisson ratio was found to have only a small effect; a larger Poisson ratio tended to reduce strains at intermediate pressures and increased them at higher pressures. It is concluded from the studies with a bilinear material law that, where a multi–linear material model is not available, a 'tangent modulus' model, i.e. a straight line between the yield limit and the ultimate strength, is most accurate when the high strains are localized. An increase in the strength of the weld material was found to reduce the deformation in the base; this is consistent with test observations.

The last two overpacks were not analysed by finite element calculations. Overpack I4 was geometrically identical to the standard overpack I1, but with electro–beam welds used throughout instead of TIG welds. Overpack I4 failed in a manner very similar to that of I1 but buckling occurred at a lower pressure (Table 9). As the welding method was the only parameter which differed from overpack I1 to I4, this implies that TIG welding leads to a stronger overpack than electro–beam welding. This can be explained by noting the larger and hence stronger heat affected zone of the former.

Overpack I5 represents a heavily corroded overpack. Craters were formed by electrolysis in the surface of the overpack; they had an average surface area of approximately 500 mm^2 and a local reduction in the wall thickness of up to 50 %, although the average thickness reduction was only 5 %. Comparison of the experimental results with those for overpack I1 indicates that the reduction in failure pressure due to the simulated corrosion is nearer to the average reduction in wall thickness than to the maximum reduction.

Table 10: Failure prediction for the advanced testwork.

Overpack	A0	A1	A2	A3
Description	Stan-dard	Reduced wall thick.	Pre–de-formed body	Pre–def., cracked body
Length of body [mm]	600	400	600	600
Outside diameter [mm]	200	156	210/190	210/190
Wall thickness [mm]	36	14	30	30
Crack	–	–	–	long.
Experimental data				
Failure pressure [MPa]	–	65	111	105
Buckling mode [lobes]	–	2	2	2
OAP				
Failure pressure [MPa]	–	67	108	107
Buckling mode [lobes]	–	2	2	2
SCK–CEN				
Failure pressure [MPa]	–	–	–	–
Buckling mode [lobes]	–	[1)]	–	–
CEA				
Failure pressure [MPa]	–	65	85	54
Buckling mode [lobes]	–	3	2	2
ENSA				
Failure pressure [MPa]	–	59	82	78
Failure	–	Plastic hinge	Collapse	Collapse
Location		Body/Base	Body	Body
PSI/NAGRA				
Failure pressure [MPa]	–	68	96	96
Buckling mode [lobes]	–	3	2	2

[1)]: No buckling calculation was performed.

1.5 Advanced tests on scale models of typical overpacks

This series of tests is on models of overpacks with realistic details (such as end closures) (OAP 1990b). A reference overpack design was produced (Fig. 1.4b) as being a true one–third scale model similar to the NAGRA reference design (Fig. 1.4c). This reference overpack was designed with a realistic diameter to thickness ratio (and consequently would be too strong to test in the available test facilities) and was the basis for variations for testing. Three variants on the reference design were chosen (Table 10), one with thinner walls and two with predeformed walls. The specimens with

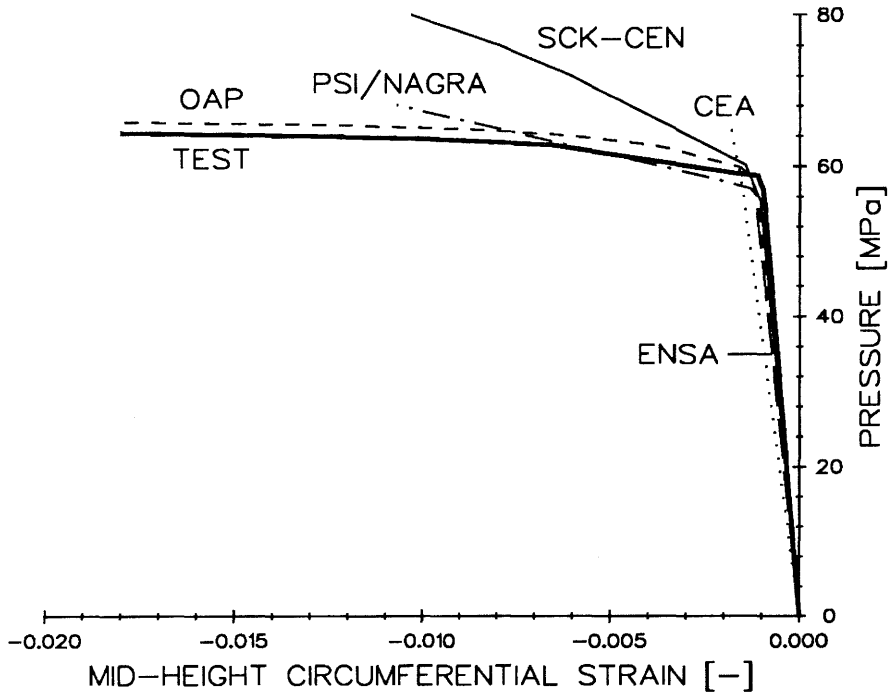

Fig. 1.6: Mid–height circumferential strain of overpack A1 in the advanced testwork.

predeformed walls were similar to the reference overpack but with the walls deformed so that they varied from circular at the ends to elliptical at the centre. The body, lid and base of each overpack were machined from the same steel bar. Each overpack was tested in a pressure chamber capable of pressures up to 140 MPa. In all tests the temperature was controlled at 20 °C.

The overpacks A2 and A3 were very close to buckling, but no evidence of tensile failure or of a weakening at the lid/body or body/base interface was observed. The longitudinal crack machined on overpack A3 has little effect on overpack performance before yield. However, it appears to lower the final failure pressure. This reduction is due to the reduced strength of the wall, rather than crack growth.

The partners' agreement with the test data is good over the elastic range of the material for the overpack A1. The overpack material in the mid–height section yields at a pressure of about 60 MPa and controlled plastic deformation occurs up to a pressure of about 63 MPa (Fig. 1.6).

The predictions were not as accurate for overpack A2 as they were for overpack A1. Strains measured on the minor axis are an order of magnitude greater than the corresponding strains on the major axis throughout the elastic region (Fig. 1.7). OAP and PSI/NAGRA match the test data in the initial region well; they indicate beyond yield the correct form of the strain history curve showing rapid increase in compression strains up to failure. However, the pressures at which yield is predicted are significantly lower

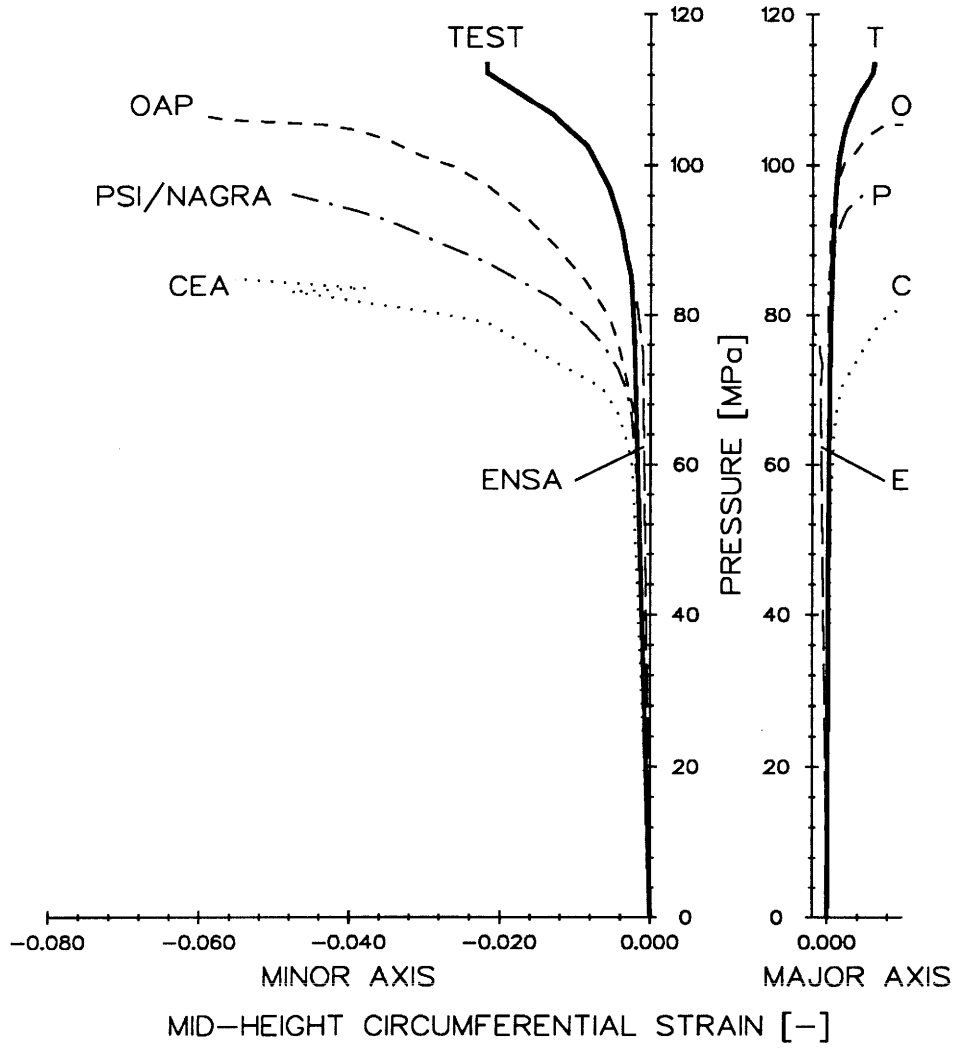

Fig. 1.7: Mid–height circumferential strain of overpack A2 at the minor and the major axis in the advanced testwork.

than found in the experiments.

Overpack A3 behaved similarly to overpack A2. The behaviour predicted by OAP and PSI/NAGRA appears at first sight to be more accurate for overpack A3 than their results for the previous overpack A2. However, close comparison of the results for A2 and A3 indicate that the crack has been predicted to have little effect on the behaviour of the overpack (1 MPa), whereas the test results indicate a 5 MPa drop in failure pressure as a result of the crack. It is therefore not that the results for overpack A3 are more accurate but rather that there was an insufficient mesh density around the crack to adequately represent the stress concentrations in this area. Examination of sections through overpack A3 after testing showed no evidence of crack growth. This was confirmed by an additional elastic fracture mechanics calculation by PSI/NAGRA; fracture would not be reached until pressures far in excess of the buckling load were applied.

2 Thermomechanical calculation of residual stresses due to welding using the finite element method

2.1 NAGRA reference design for the high level nuclear waste overpack

The design work carried out (NAGRA 1984 and STEAG & MOTOR–COLUMBUS 1984) led to the NAGRA reference design shown in Figure 2.1. The overpack consists of a cylindrical body with integrated hemispherical bottom and pre–assembled additional shielding; a hemispherical lid, also with pre–assembled additional shielding and with a thread for a gripping device, is pressed onto the body and held in place by means of a conical thread and subsequently welded. The sole aim of weld is to tighten the overpack.

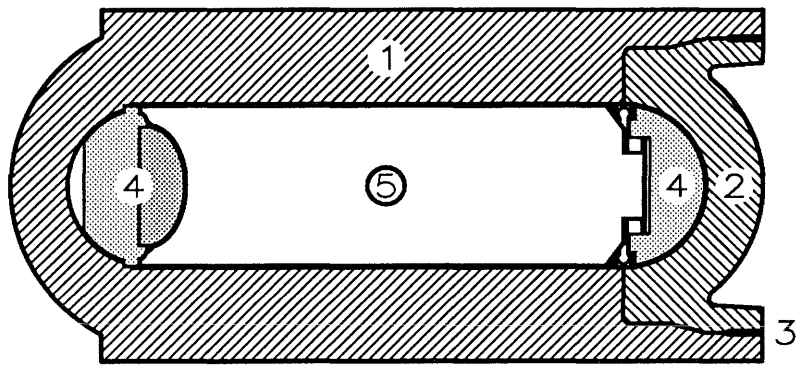

Fig. 2.1: The basic features of the NAGRA reference overpack. (1) overpack body, (2) overpack lid, (3) weld, (4) additional shielding, (5) space for accomodating waste cylinder.

The stress analyses were carried out by STEAG & MOTOR–COLUMBUS (1984) in conformity with the ASME–Code, Section VIII, Division 1 for a wall thickness reduced by the amount of the design corrosion allowance of 50 mm. It was assumed that the backfill exerts an isostatic pressure of approximately 30 MPa on the overpack; the 30 MPa correspond to the maximum swelling pressure of the compacted bentonite used as backfill material. This load resulted in maximum stresses of 80 MPa, i.e. a margin of a factor 5 was reached against the ultimate tensile strength of 400 MPa for GS-40 cast steel. Furthermore, these stresses were shown to be compressive almost everywhere, external tensile stresses being limited to the area of the weld and not exceeding 10 MPa. However, stresses induced by the welding process were not considered.

It should be noted that higher tensile as well as compressive stresses would have to be expected if the external loads are inhomogeneous, as in the un-

Table 11: Chemical composition of GS-40 cast steel (in weight percent (SIMPSON 1984)).

C	P	S	Si	Mn	Al	Fe
0.19	0.014	0.006	0.37	0.74	0.06	balance

likely case of an inhomogeneous swelling of the bentonite. However, even those stresses would be considerably smaller than the residual stresses induced by the welding procedure. In this respect it is worth emphasizing the fact that in the NAGRA reference design no full heat treatment is foreseen after emplacement of the vitrified waste and closure of the overpack. The reason for this is that exposure of the borosilicate glass waste matrix to elevated temperatures for extended periods of time may lead to a partial recrystallization of the glass, resulting in higher leaching rates in groundwater after eventual failure of the overpack.

2.2 Material properties

2.2.1 GS-40 cast steel

A relatively low–strength (400 MPa ultimate tensile strength) cast steel of type GS-40 (essentially equivalent to US Standard ASTM A27–Grade U 60-30) was chosen as the overpack reference material (Table 11). Cast steel is normally used instead of cast iron when a good weldability or a higher toughness due to shock–like loadings is demanded. The characteristic property of cast steel is its guaranteed minimum tensile strength which in general is given in the identification number. Other mechanical parameters can be guaranteed up to 300 °C according to the standard DIN 1681 for example.

The required long–term corrosion resistance is ensured for the NAGRA reference overpack by the principle of a mechanical stable overpack which is constructed out of a base material with an allowable small corrosion rate, i.e. where the remaining wall thickness at the end of the design lifetime is still large enough to ensure mechanical stability and tightness. Experiments showed (SIMPSON 1984) for GS-40 cast steel a corrosion allowance of 50 mm, which would be adequate to cover both general corrosion and pitting corrosion. The rationale behind the choice of a low–strength steel is that potential problems associated with stress corrosion cracking would be minimized. Ease of manufacture and quality control, e.g. at the weldings, are further advantages of a corrosion–resistant base material such as GS-40 cast steel.

Table 12: Tensile properties of GS-40 cast steel (ROSSELET 1988).

Temperature T [°C]	strain rate	20	400	700	900
Yield limit	$3{\cdot}10^{-4}$/s	248	158	59	28
$Rp_{0.2}$ [MPa]	$3{\cdot}10^{-3}$/s	264	158	72	34
Ultimate strength	$3{\cdot}10^{-4}$/s	442	355	67	42
Rm [MPa]	$3{\cdot}10^{-3}$/s	475	376	95	60
Elongation at rupture	$3{\cdot}10^{-4}$/s	28	39	82	36
A [%]	$3{\cdot}10^{-3}$/s	29	31	82	71
Reduction of area	$3{\cdot}10^{-4}$/s	56	67	89	29
Z [%]	$3{\cdot}10^{-3}$/s	57	59	95	63

2.2.2 Uniaxial tension tests

Material properties for GS-40 cast steel at elevated temperatures and for the weld material, which is assumed to behave like the parent material, are very scarce in the literature. Therefore, uniaxial tension tests were performed on GS-40 cast steel at temperatures up to 900 °C (ROSSELET 1988) and at two different strain rates. The experimentally determined tensile parameters are summarized in Table 12.

Three uniaxial tension tests were performed for each temperature (20 °C, 100 °C, 200 °C, 300 °C, 400 °C, 500 °C, 600 °C, 700 °C, 800 °C and 900 °C) on samples with a diameter of 10 mm and a gauge length of 50 mm. The force–elongation curves obtained were digitized and averaged. They were then transferred into true stress–strain curves according to the following formulae and the assumption of volume constancy during plastic deformation:

$$\varepsilon = \int_{L_0}^{L} \frac{dl}{l} = \ln \frac{L}{L_0}$$

$$\sigma = \frac{F}{A} = \frac{F}{A_0} \cdot \frac{A_0}{A} = \frac{F}{A_0} \cdot \ln \frac{L}{L_0}$$

where: L_0 : initial gauge length (50 mm)

L : current length

F : force

A_0 : initial area (78.54 mm^2)

A : current area

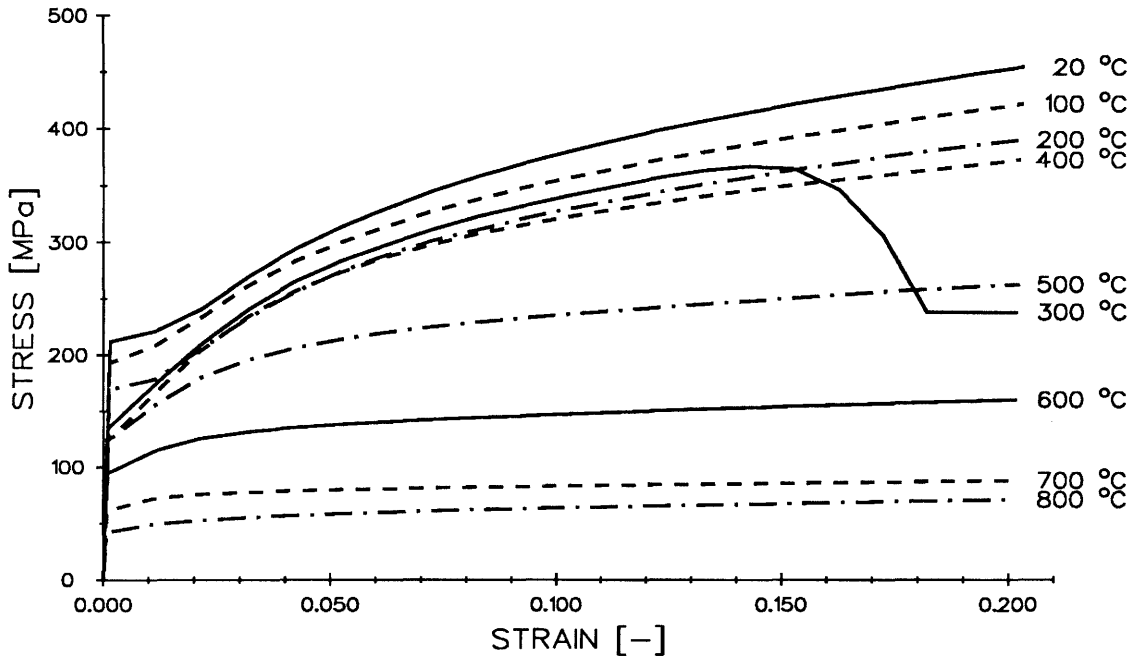

Fig. 2.2a: Uniaxial tension tests on GS-40 cast steel at a strain rate of $3 \cdot 10^{-3}$ s^{-1} (after ROSSELET (1990)).

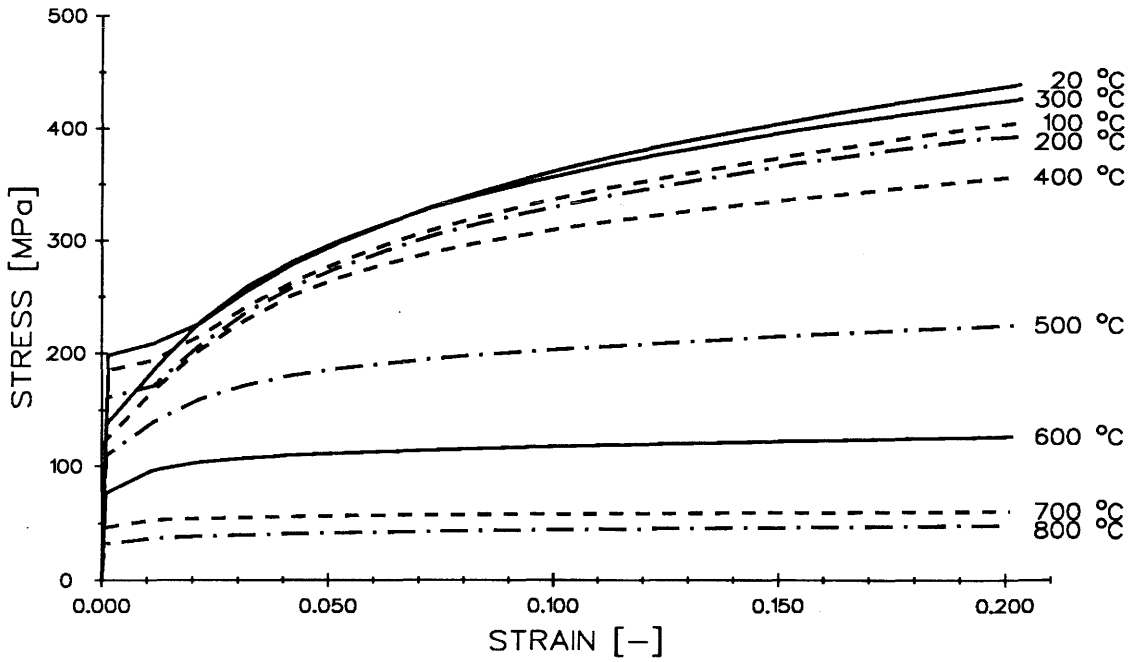

Fig. 2.2b: Uniaxial tension tests on GS-40 cast steel at a strain rate of $3 \cdot 10^{-4}$ s^{-1} (after ROSSELET (1990)).

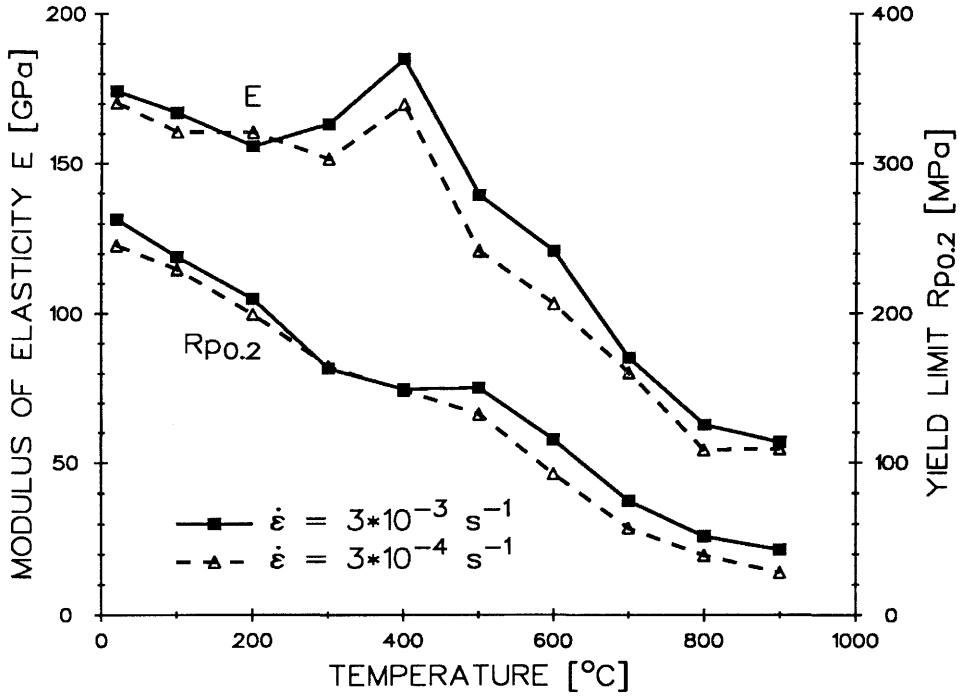

Fig. 2.3: Temperature dependency of the modulus of elasticity E and the yield limit $Rp_{0.2}$ (ROSSELET 1990).

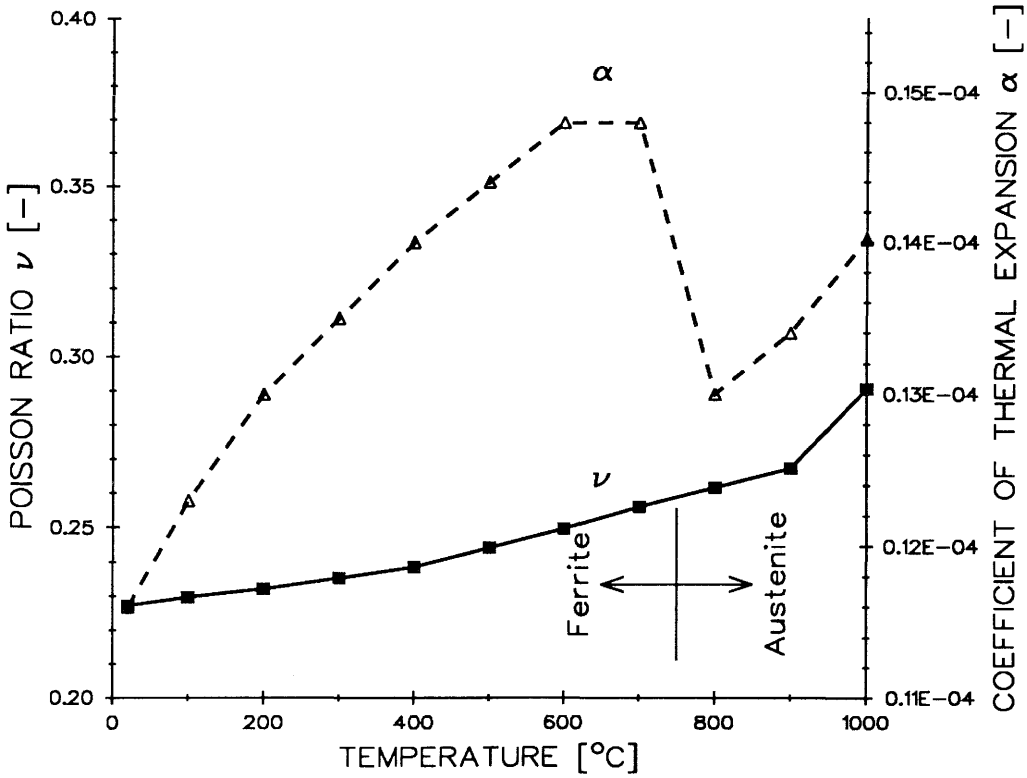

Fig. 2.4: Temperature dependency of the Poisson ratio ν and the coefficient of thermal expansion (RICHTER 1973).

The (true) stress–strain relations from the experiments for the two strain rates are shown in Figure 2.2; the curves at 900 °C match those at 800 °C and therefore are not included in the figures. The temperature dependency of the modulus of elasticity E and the yield limit $Rp_{0.2}$ is given in Figure 2.3. The two further parameters which are necessary for a time independent, thermomechanical calculation, i.e. the Poisson ratio ν and the coefficient of thermal expansion α, are represented in Figure 2.4. The values of these parameters are taken from (RICHTER 1973) for a weldable fine–grained steel. The coefficient of thermal expansion α is reduced at 800 °C, thus indicating some transformation plasticity at the ferrite–austenite transformation.

2.2.3 Creep tests

In this work, creep is understood as a flow which is time dependent and which is possible for any stress; yielding is understood as a flow which arises only when the stress is above a certain threshold level, namely the yield limit.

The influence of creep on the material behaviour increases with increasing temperature; at temperatures such that the creep response time, even under low stresses, is smaller than the time constant of the temperature history, only small stresses can build up. It is therefore necessary to estimate the limiting temperature below which creep can be neglected for time horizons of the order of the duration of the cooling period after completion of the weld: significant residual stresses can build up only below that temperature.

In order to address this issue, to determine the creep behaviour of GS-40 cast steel and to develop an adequate mathematical description of the primary and secondary creep, a series of creep tests under constant loading were carried out on samples (diameter 8 mm, gauge length 38 mm) of GS-40 cast steel at the three temperatures 400 °C, 550 °C and 700 °C (ROSSELET 1990). Figure 2.5 shows the creep curves obtained in the tests. It can be seen that already at 400 °C the primary creep rate is important. Also at this temperature an important strain hardening is observed, i.e. the creep rate decreases rapidly with time (Figure 2.5a). By contrast, at 700 °C (Figure 2.5c), the strain hardening is practically compensated by the recovery and primary creep is not observed.

2.2.4 Implementation of the material properties into a finite element calculation

The time independent stress–strain relations are represented in the finite element calculations either by a multilinear, temperature– and strain rate–dependent or by a bilinear, temperature–dependent material law. The former is implemented into the material model by a table, the latter is given by the input. The bilinear material law is based on the experimental values with a

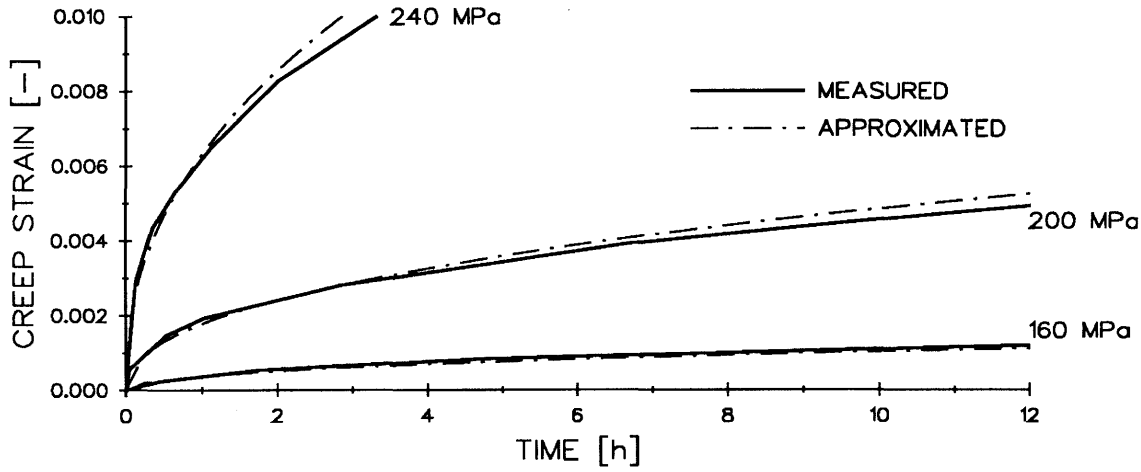

Fig. 2.5a: Creep experiments on GS-40 cast steel at 400 °C.

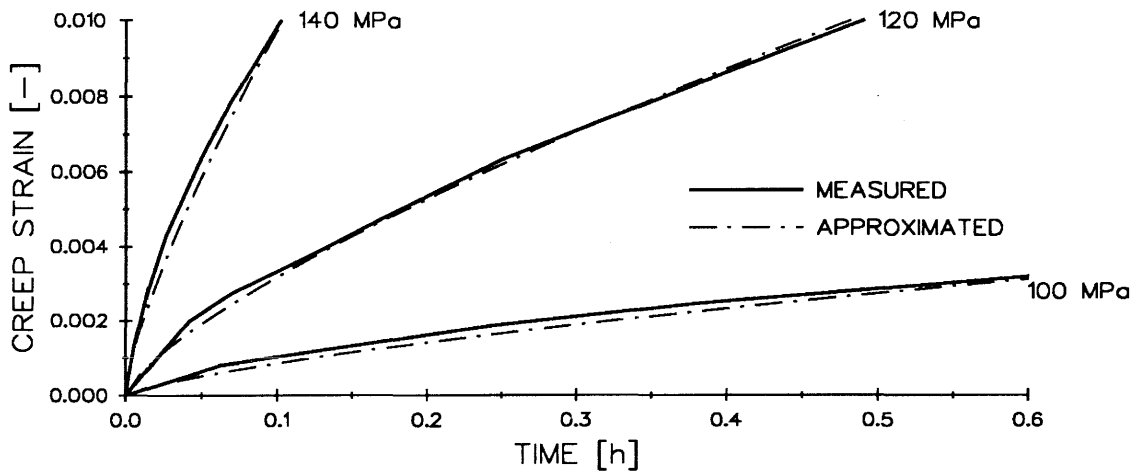

Fig. 2.5b: Creep experiments on GS-40 cast steel at 550 °C.

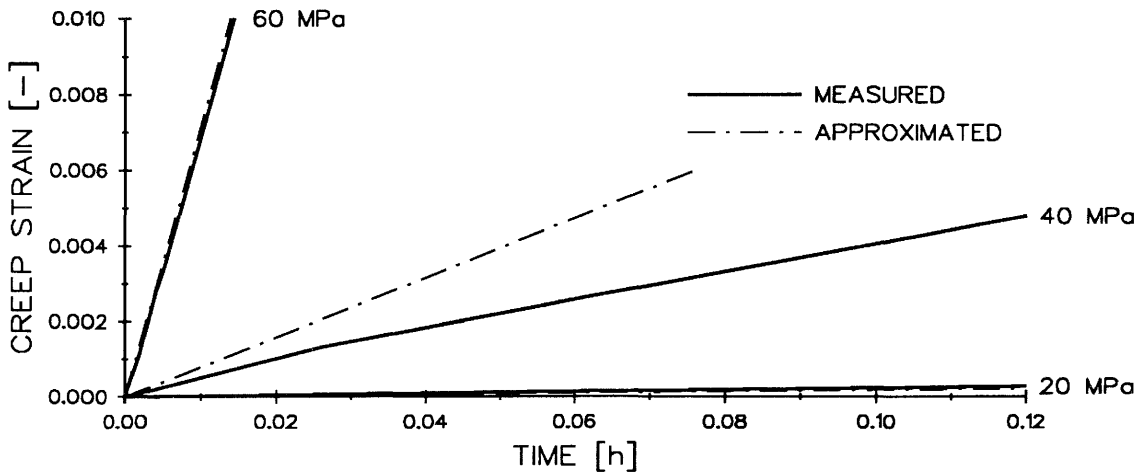

Fig. 2.5c: Creep experiments on GS-40 cast steel at 700 °C.

strain rate of $3 \cdot 10^{-4}$ s^{-1} and a linear regression analysis for the part of the curves with plastic deformation and strains up to 10 %.

The molten material is simulated by a solid without strength, volume constancy and no thermal expansion. Its material properties are chosen in a bilinear material model according to the following assumptions:

$E_{melt} = E_{900\ °C}$	The modulus of elasticity E_{melt} is kept constant at a rather high value to avoid possible numerical instabilities in the finite element calculations.
$Rp_{0.2,\ melt}$ = 0.1 MPa H_{melt} = 0.0 MPa	The liquid without strength state is replaced by a low strength solid (due to numerical instabilities) without hardening. The yield limit $Rp_{0.2,\ melt}$ defines the strength since the hardening modulus H_{melt} is zero.
ν_{melt} = 0.48	Volume constancy is explicit by using a Poisson ratio of 0.5, a value which is set at 0.48 due to possible numerical instabilities.
$\alpha_{melt} \cdot T$ = 0.023 °C	No additional thermal expansion is reached by a constant product of the coefficient of thermal expansion α_{melt} times the temperature T; its value of 0.023 °C is independently to the reference temperature and results from an α–value at 1450 °C, which was extrapolated from the data given in (RICHTER 1973). An α_{melt} of 0.0 would result also in no additional thermal expansion but in an inconstancy of the thermal strains at solidification/liquefaction and therefore, to possible numerical instabilities.

The values of the parameters at temperatures in between the measured values (up to 900 °C) and the assumed values for the molten material (above 1450 °C) are linearly interpolated between these two boundaries.

The evaluation of the creep tests has shown that no simple, general equation exists to describe the creep behaviour. However, in an attempt to translate the creep data obtained into a form amenable to their use in computer modelling, they were fitted by regression analysis to an empirical equation according to Norton's law. One observes in Figure 2.5 an approximation of the measured data using this empirical equation. Figure 2.5c) shows for 40 MPa that an unique equation is a too rough simplification to represent the phenomena involved in a creep process.

The following empirical equation was used to fit the experimental creep data:

$$\varepsilon^{cr} = a_0 \cdot \sigma^{a_1} \cdot t^{a_2}$$

Creep strain ε^{cr} in [–], stress σ in [MPa], time t in [s]

T	a_0	a_1	a_2
400 °C	5.15E-21	6.950	0.435
550 °C	3.26E-18	7.275	0.730
700 °C	4.07E-14	5.450	1.000

Instead of an empirical equation, it would be preferable to work with a mathematical simulation model which combines the different physical processes and their interactions with the creep equation. This mathematical simulation is presented in more detail in ATTINGER et al. (1991), but it is too extensive to be implemented into a finite element programme. Therefore, it will not be used in this work.

The current values of the material properties are assumed to be constant over a time step. They are determined by interpolation from the values in the table or from the input for the temperature T within the time step according to the iteration factor α':

$$T = T_0 + \alpha' \cdot (T_E - T_0)$$

where T_0 : temperature at the beginning of the time step
T_E : temperature at the end of the time step

The strain rate at the beginning of the time step is used when strain rate effects are considered. The material parameters are linearly interpolated between the measured values for a strain rate in between the measured rates ($3 \cdot 10^{-4}$ s^{-1} and $3 \cdot 10^{-3}$ s^{-1}) and taken as the values at the corresponding boundary for a rate beyond the measured rates.

2.3 Study on some fundamental aspects of modelling stresses induced by welding

2.3.1 One–dimensional modelling of the welding process

As a first step, the one–dimensional FIBRE model will be discussed. This model should give an insight into the parameters involved in the thermomechanical analysis of a welding process.

The FIBRE model is constructed according to the commonly used separation of total strain into its elastic, plastic and viscous part, i.e. $\varepsilon^{tot} = \varepsilon^{el} + \varepsilon^{pl} + \varepsilon^{vi}$, where each part is loaded by the same stress σ. If one continues with the modelling, each part is replaced by its symbolic element, i.e. by a spring, slider and dashpot respectively. The arrangement of these elements in a chain will form a fibre. The fibre of unit length is fixed on both sides and is heated up. It will be loaded as a result of the temperature induced elongation,

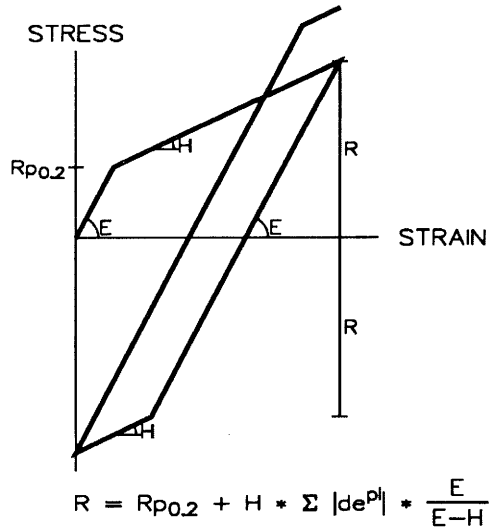

Fig. 2.6a: Isotropic hardening.

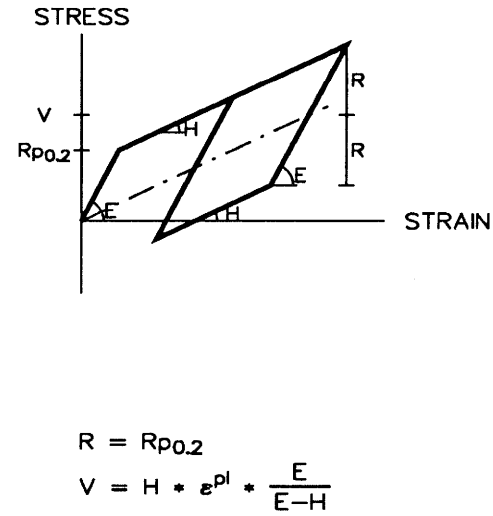

Fig. 2.6b: Kinematic hardening.

which is given by the product of the coefficient of thermal expansion α times the temperature T, and each element is strained following its material law. A temperature dependent Hook's law is assumed for the elastic element, the spring. It is described in the one–dimensional case by the modulus of elasticity E:

$$\sigma = \varepsilon^{\mathrm{el}} \cdot E.$$

The slider represents plasticity. Deformation occurs when the stress overcomes a certain temperature dependent stress level, the yield limit $Rp_{0.2}$; the slider will then harden either isotropically or kinematically. The current 'yield limit' grows according to its hardening modulus H and the summed up plastic strain increments in the case of isotropic hardening (Fig. 2.6a). Since the plastic strain increments are also summed up during reversed loading, a reloading will result in a higher current 'yield limit' and a stress vs. strain loop cannot be closed. The initial yield limit is shifted in the case of kinematic hardening (Fig. 2.6b); therefore, reloading will result in a closed loop. Deformation in the molten state may lead to large plastic strains and thereafter to a considerable hardening in the solid state. To circumvent this, a modification to the hardening law is proposed at the solidifying stage of the molten material; the past hardening is reset to zero.

The temperature dependent Norton's law is assumed for the dashpot, thus representing secondary creep: $\varepsilon^{\mathrm{vi}} = B \cdot \sigma^n \cdot t$. This exponential law, with n normally above 1.0, poses some numerical problems in the determination of the viscous strain $\varepsilon^{\mathrm{vi}}$ when it is large, i.e. when $\varepsilon^{\mathrm{vi}}$ is greater than about $0.1 \cdot \varepsilon^{\mathrm{el}}$. When one starts from the given strain $\varepsilon^{\mathrm{tot}}$ and assumes full elasticity in a first step, then it is obvious from Figure 2.7, that a numerical overflow may occur due to the large viscous strain at high stress. Another method is to start the iteration from the assumed stresses σ_1 and σ_2. The next stress may

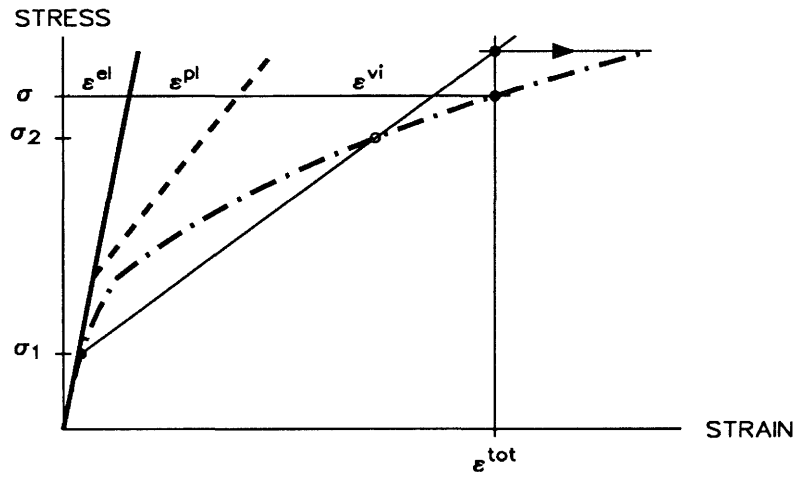

Fig. 2.7: Iteration procedure for visco elasto–plastic material behaviour.

be guessed from an extrapolation to the strain ε^{tot} as shown in Figure 2.7. This procedure is unsafe when small stresses are assumed for a large ε^{tot}. Interpolation is also not in place due to a bad convergence in some cases.

What remains is the simple trial and error method according to the 'regula falsi' as shown in the flow chart of the FIBRE programme (Fig. 2.8), where the above equations are written in an incremental form for a time increment dt. Since the FIBRE programme has to explain the effect of the different parameters involved in a thermomechanical calculation, no effort was put into an accurate time integration or into an evaluation of its iteration algorithms.

2.3.2 Material properties and loading

The thermo elasto–plastic material behaviour was taken as defined in section 2.2 (material properties). Three different material property sets were investigated; they differed in terms of the viscosity parameters. Material property set 1 is thermo elasto–plastic, the material property sets 2 and 3 are visco thermo elasto–plastic, whereby material property set 2 is more viscous at low temperature and material property set 3 more viscous at high temperature (Fig. 2.9). Between 400 °C and 700 °C material property set 2 uses in the creep parameters determined for GS-40 cast steel at a time t of 1 s.

The loading of the fibre is a function of the temperature and three types of temperature evolutions are considered. The first one consists of 3 cycles, one of which is shown in Figure 2.10. This form is a rough approximation of the temperature evolution as it was determined for the welding of the overpacks (MEYER & ATTINGER 1987). The second and the third type of loading have the same form and temperature as the first one, but the time axis is delayed by a factor of 10 and 100, respectively.

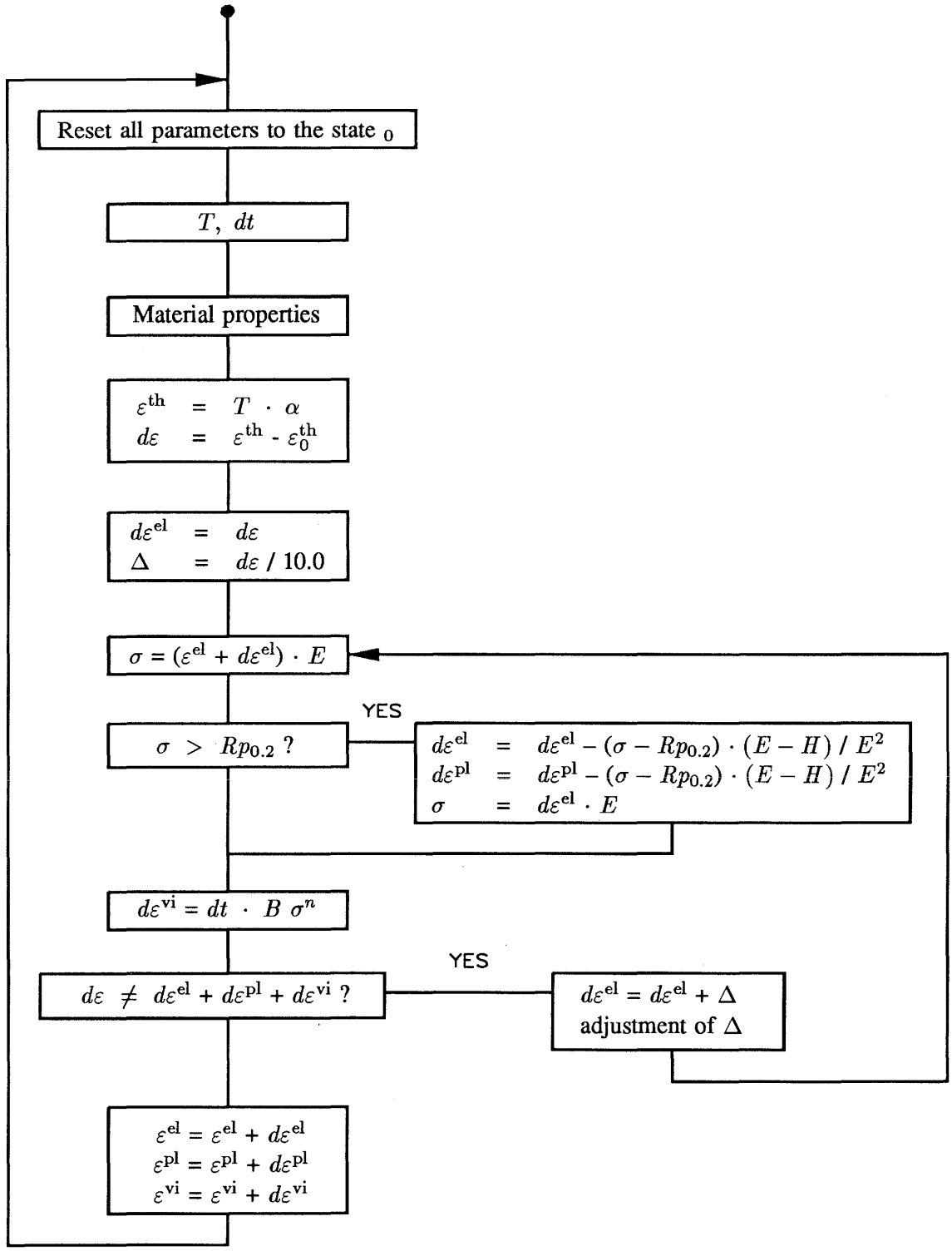

Fig. 2.8: Flow chart of the FIBRE programme.

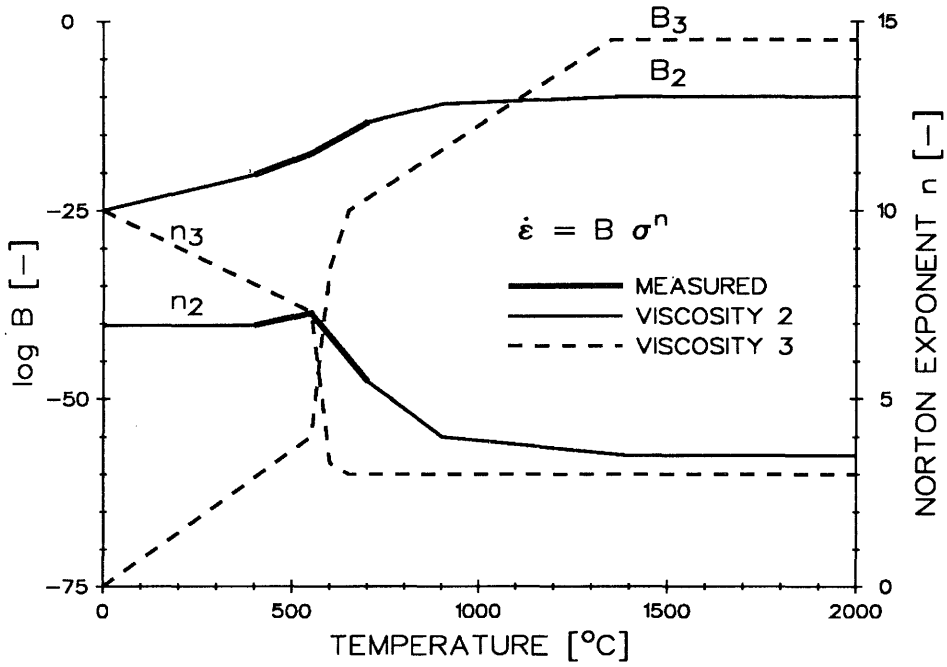

Fig. 2.9: Temperature dependency of the viscosity parameters for material property set 2 and material property set 3.

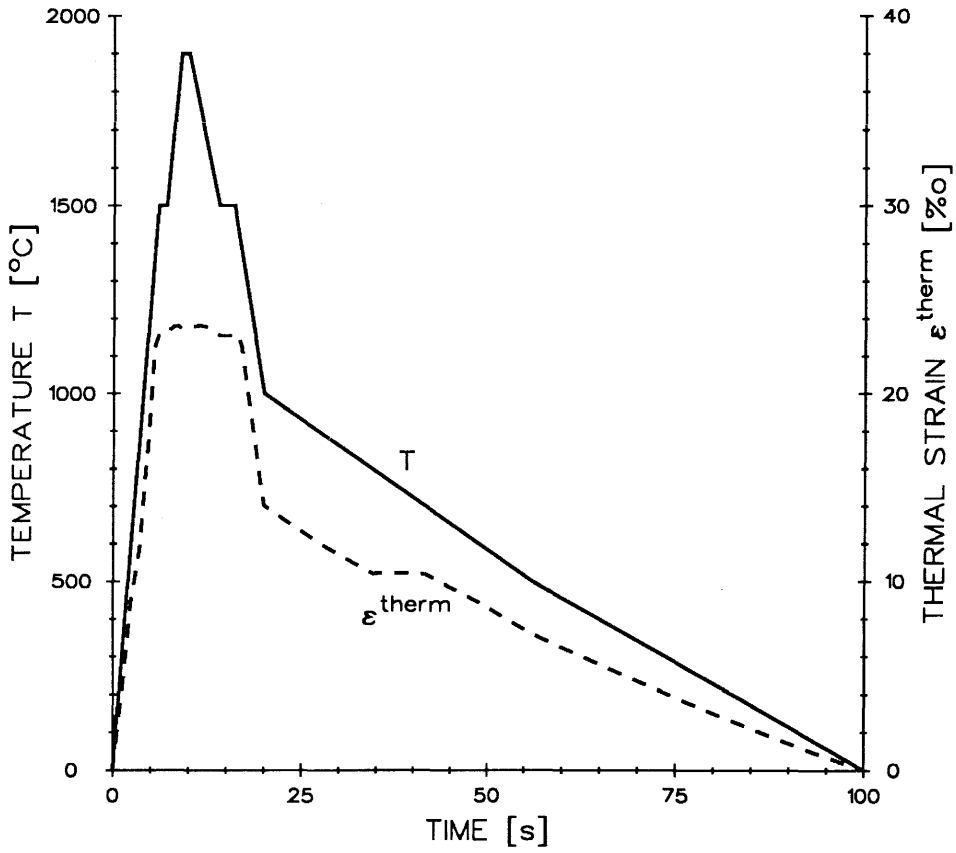

Fig. 2.10: Evolution of the temperature and the thermal strain ε^{therm} it induces.

The temperature induces the expanding thermal strain ε^{therm} (Fig. 2.10). It is constant (besides some numerical instabilities) for temperatures above 1450 °C due to the assumed values of the coefficient of thermal expansion α. Since the fibre is fixed at both ends in the FIBRE model, this strain will be compensated for by the total strain ε^{tot}. This permanent fixation is not adequate for the simulation of annealing, where restraints are largely prevented.

Following the usual conventions, tension is assumed to be positive and compression to be negative.

2.3.3 Parametric study

A parametric study was performed which considers the influence of time, material properties and hardening; Table 13 summarizes the residual stresses of these calculations. The thermo elasto–plastic calculations show the expected behaviour of the different hardening methods, i.e. isotropic hardening results in higher residual stresses than kinematic hardening and its residual stresses increase steadily with the number of loading cycles. The reset of the past hardening overcompensates the plastic strains at solidification and the residual stresses are therefore larger than kinematic hardening without resetting. Isotropic and kinematic hardening give the same results when the past hardening is reset and full loading cycles with melting are considered. One observes a slight reduction in the residual stresses when the material property set is changed from 1 to 2 and viscosity is considered. The residual stresses are further slightly reduced when the timescale is enlarged. As is demonstrated for material property set 3, a larger viscosity at high temperature may compensate the plastic strains by viscous strains and therefore overcompensates them; increased residual stresses are observed for the kinematic hardening depending on the timescale used. In general, viscosity at high temperature (material property set 3) results in residual stresses at a lower stress level than viscosity at low temperature (material property set 2). Compared to an elasto–plastic material behaviour, the residual stresses are reduced by about 11 % for the former and by about 8 % for the latter when the past hardening is reset and the timescale is greatly increased.

The evolution of the stress vs. strain during different loading cycles is depicted in Figure 2.11. The cycles match each other quite well for all material property sets. As already mentioned, isotropic hardening yields to increased residual stresses. The transformation, i.e. the reduction of the coefficient of thermal expansion α at 800 °C, results only in tension, i.e. during cooling, to an unloading for the short loading periods considered. An extended loading period allows viscous strains to grow at the expense of plastic strains, as is obvious for material property set 2 and a reset of the past hardening (Fig. 2.11). Thereby, the yield limit is reached later and the plastic strains are suppressed for longer. The material is therefore less able to harden and

the residual stresses are consequently reduced.

Table 13: Parametric study with the one–dimensional FIBRE model.

Time t_{max}	Material property set	Hardening	Residual stresses [MPa] cycle 1	cycle 2	cycle 3
300 s	1 : ε^{el}, ε^{pl}, —	kinematic, —	209.8	209.8	209.9
		isotropic, —	295.7	375.5	453.6
		kinematic, reset	251.5	251.5	251.5
		isotropic, reset	251.6	251.6	251.6
300 s	2 : ε^{el}, ε^{pl}, ε^{vi}	kinematic, —	206.8	204.2	201.9
		isotropic, —	281.5	342.7	400.9
		kinematic, reset	243.1	243.1	243.1
		isotropic, reset	243.1	243.1	243.1
3000 s	2 : ε^{el}, ε^{pl}, ε^{vi}	kinematic, —	206.4	203.2	200.2
		isotropic, —	270.7	323.8	372.7
		kinematic, reset	237.2	237.2	237.2
		isotropic, reset	237.3	237.3	237.3
30000 s	2 : ε^{el}, ε^{pl}, ε^{vi}	kinematic, —	205.1	200.8	197.0
		isotropic, —	261.4	303.3	343.6
		kinematic, reset	231.9	231.9	231.9
		isotropic, reset	232.0	232.0	232.0
300 s	3 : ε^{el}, ε^{pl}, ε^{vi}	kinematic, —	210.5	211.3	212.2
		isotropic, —	248.2	281.1	312.8
		kinematic, reset	228.7	228.7	228.7
		isotropic, reset	228.7	228.7	228.7
3000 s	3 : ε^{el}, ε^{pl}, ε^{vi}	kinematic, —	212.4	215.1	217.8
		isotropic, —	242.4	268.7	291.9
		kinematic, reset	227.5	227.5	227.5
		isotropic, reset	227.5	227.5	227.5
30000 s	3 : ε^{el}, ε^{pl}, ε^{vi}	kinematic, —	210.9	212.0	212.9
		isotropic, —	235.6	250.8	258.0
		kinematic, reset	223.7	223.7	223.7
		isotropic, reset	223.7	223.7	223.7

The evolution of the stresses and strains is quite similar in the different cycles for the thermo elasto–plastic material behaviour of material property set 1 (Fig. 2.12). The influence of the hardening law is small for the strains; however, kinematic hardening results in compressive plastic strains at the end of a loading cycle and therefore reduces the current yield strength. The heating phase produces an initial large stressing, the elastic strain ε^{el} and the stress are then reduced according to the reduction of the yield limit $Rp_{0.2}$, whereas the plastic strain is increased. All the calculated values are constant (besides some numerical instabilities) when the material is molten.

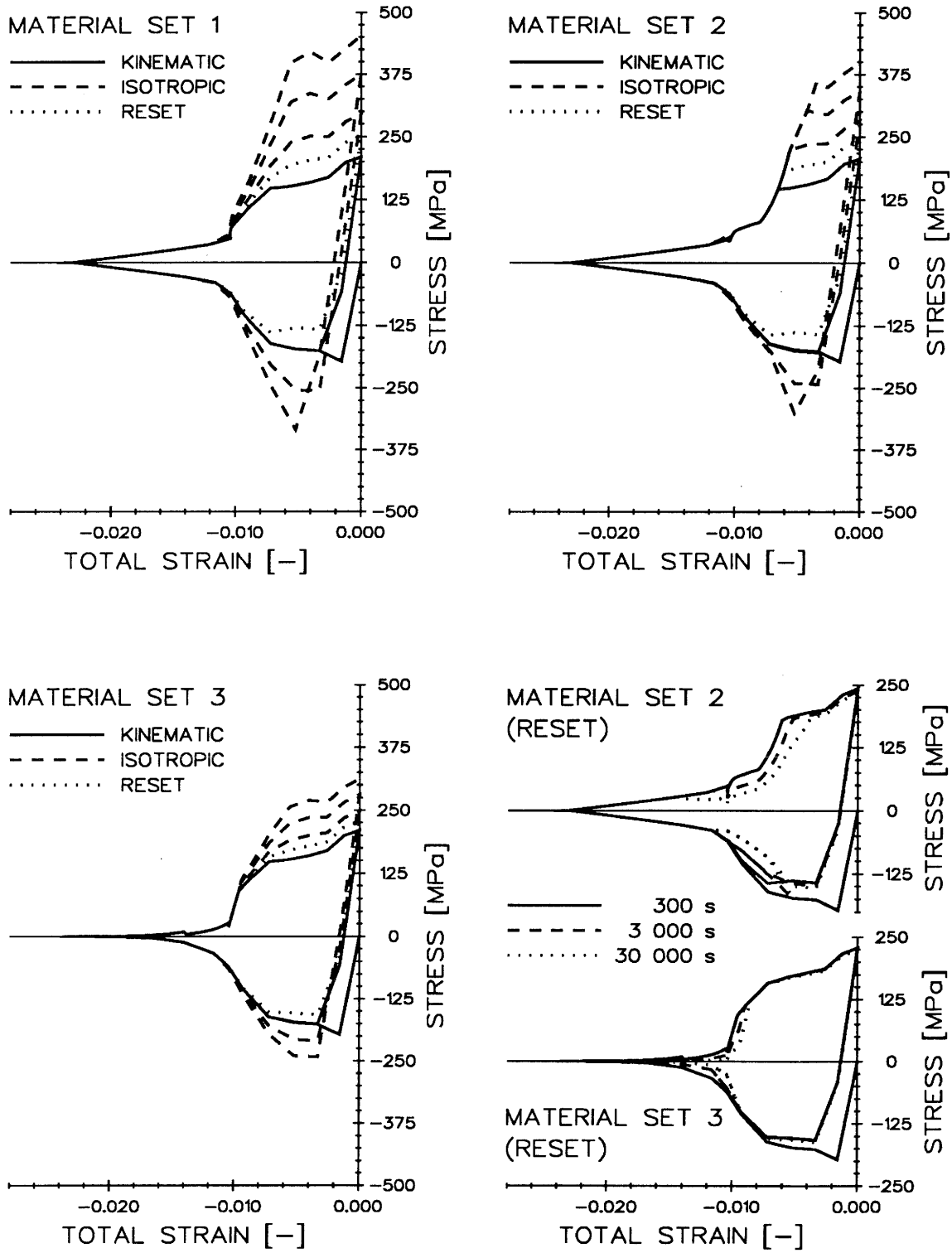

Fig. 2.11: Stress vs. total strain during different loading cycles for material property set 1 (thermo elasto–plastic), material property set 2 (viscous at low temperature, representing GS-40 cast steel) and material property set 3 (viscous at high temperature).

The transformation from austenite to ferrite is accompanied by an elastic unloading and reloading; no plastic strains are produced in this phase since the unloading is small. The stress follows the temperature dependent yield limit $Rp_{0.2}$ during the rest of the cycle.

The viscosity introduced by material property set 2 (Fig. 2.13) has a small effect on the stress and strains during heating; the fast loading rate together with a small stress at high temperature provokes only some viscous strains during part of the heating phase. During the cooling phase, most of the deformation is taken up by plastic strains at still relatively high temperatures since viscous strains are small due to the small stress. The transformation phase shows a more pronounced unloading compared to the elasto–plastic material behaviour. Viscous strains prevent the occurrence of plastic strains down to a temperature of about 500 °C. The deformations are due mainly to plastic strains during the rest of the cycle.

The influence of an extended loading period is shown in Figure 2.14 for material property set 2 and when the past hardening is reset at solidification. The longer the time period is, the more pronounced the effect of the viscous strain. The transformation from ferrite to austenite may now also be observed during the heating phase by an unloading and reloading. The evolution of plastic strains is prevented in a broader temperature range during the cooling phase, i.e. from about 1000 °C down to about 250 °C. Nevertheless, the viscous strains diminish at a too large thermal strain; the remaining unloading suffices to reach the yield limit.

The viscosity at high temperature of material property set 3 prevents the evolution of plastic strains above about 700 °C (Fig. 2.15) but has almost no effect for temperatures below this limit. An extended loading period influences the stress and strains only slightly (Fig. 2.16); the transformation from ferrite to austenite may now also be observed by an unloading and reloading during the heating phase.

The yield limit is reached at the end of a loading cycle. Viscous strains may prevent the evolution of plastic strains over a large part of the loading cycle and thereby reduce the hardening. Therefore, the lowest residual stress seems to be reached when no hardening occurs, i.e. a lower limit is given by the yield strength $Rp_{0.2}$ at the final temperature. This would result in a residual stress of about 210 MPa for GS-40 cast steel. This lower limit is only reasonable when isotropic hardening or a reset of the past hardening at solidification is assumed. Kinematic hardening would result in compressive plastic strains at the end of a loading cycle and the current yield strength would therefore be the yield strength $Rp_{0.2}$ reduced by the plastic strain ε^{pl} times the hardening modulus H.

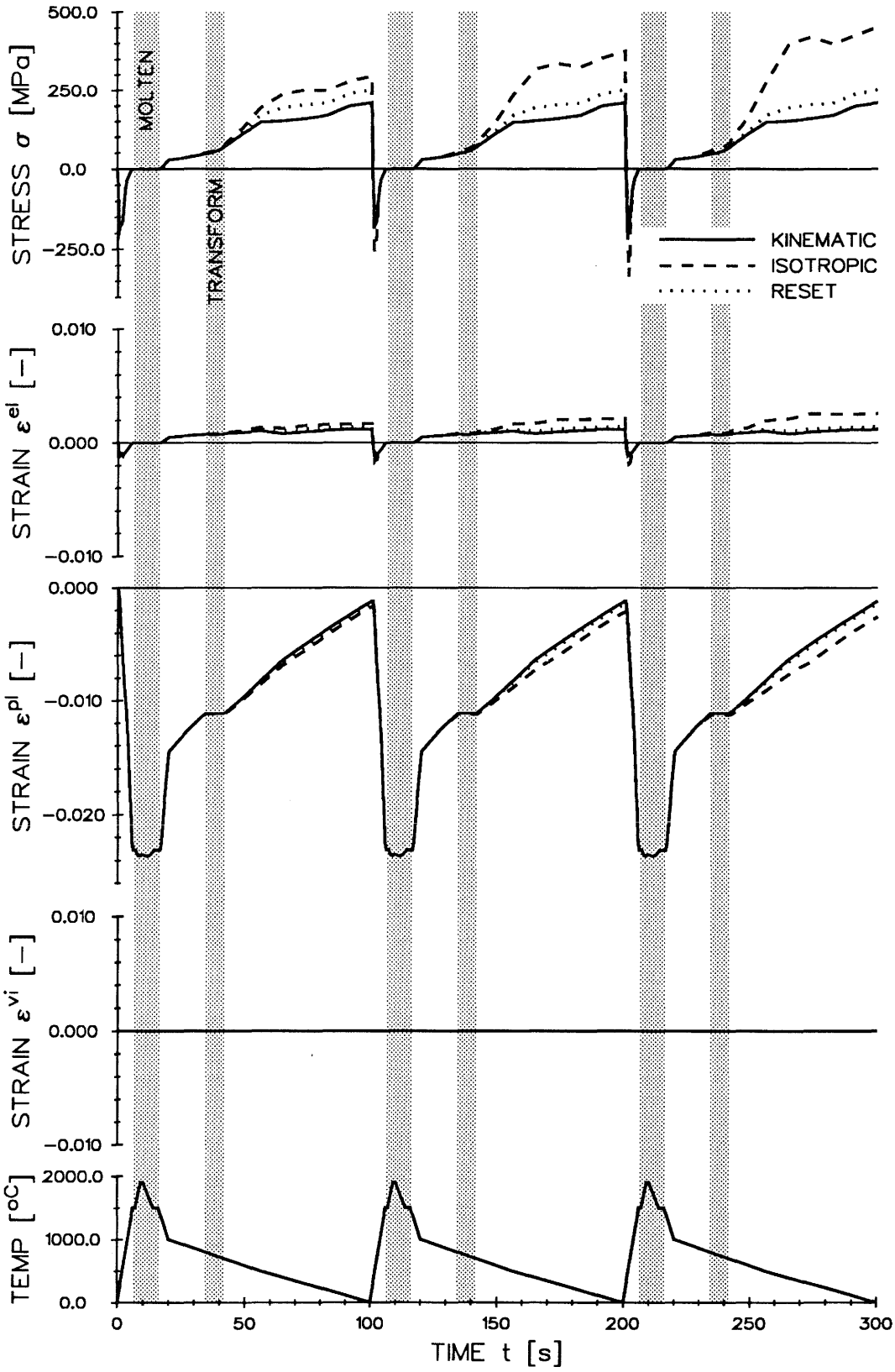

Fig. 2.12: Evolution of stress and strain for material property set 1 (thermo elasto–plastic).

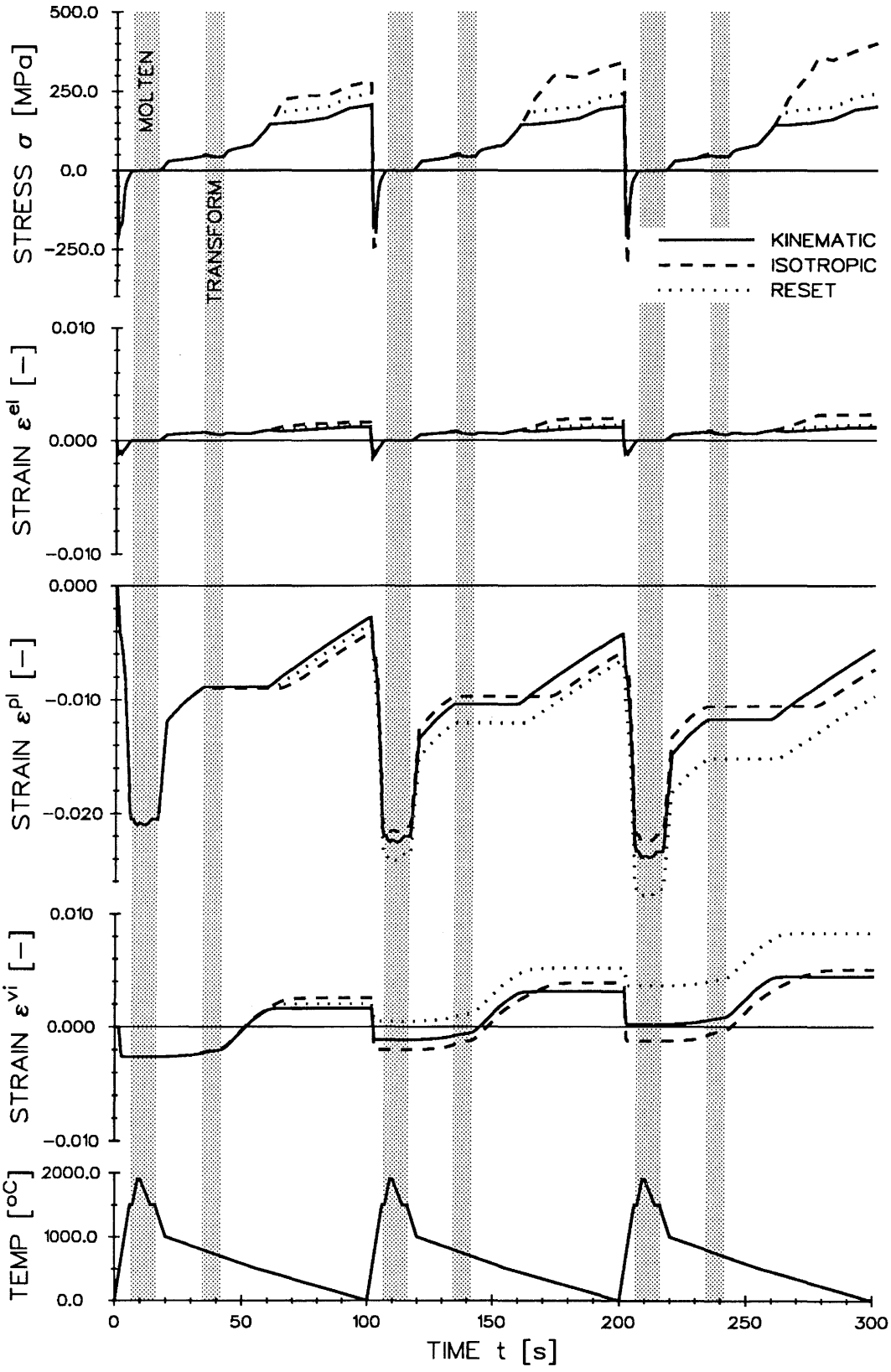

Fig. 2.13: Evolution of stress and strain for material property set 2 (visco thermo elasto–plastic with viscosity at low temperature).

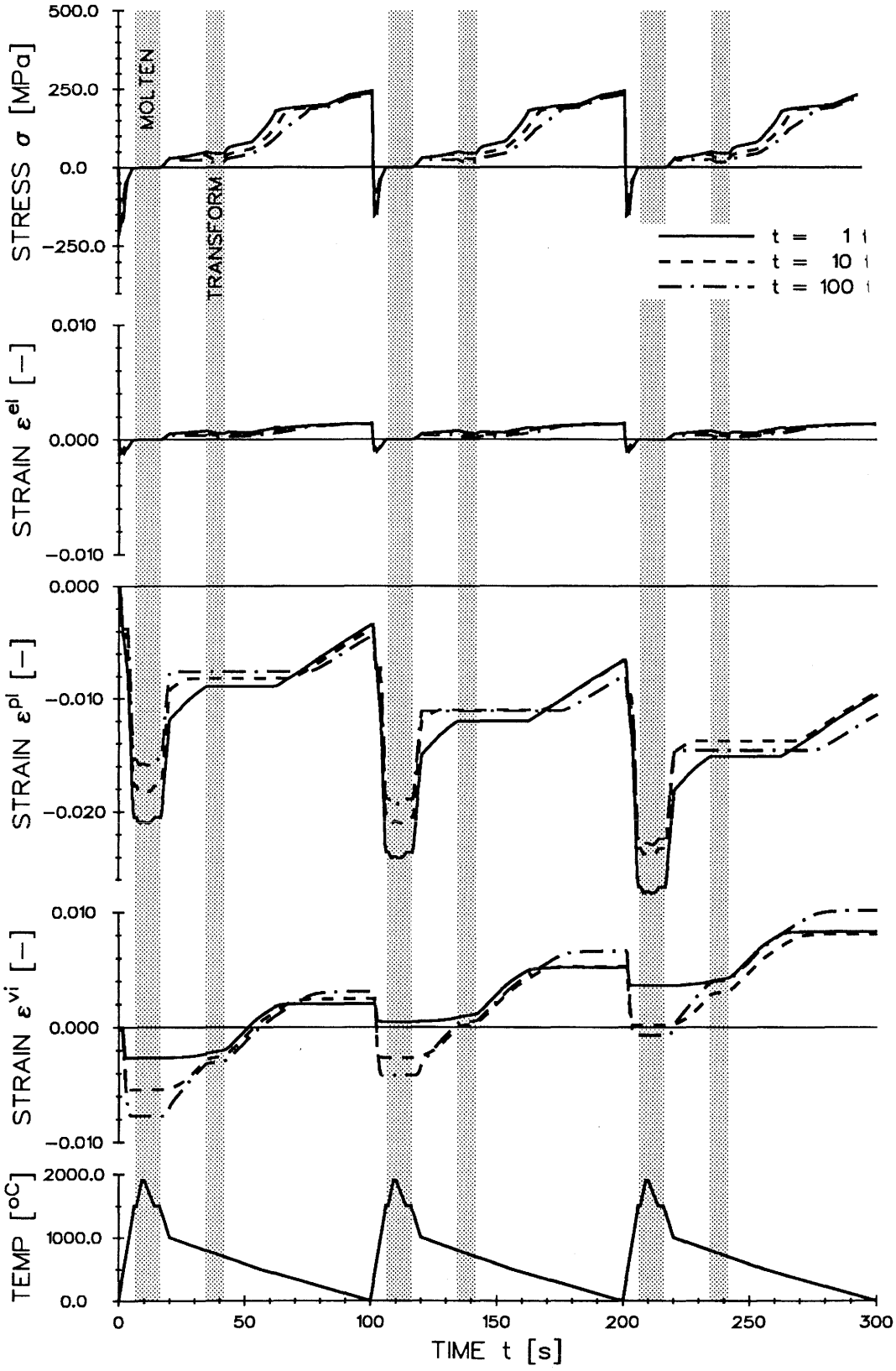

Fig. 2.14: Evolution of stress and strain for different loading periods of the temperature cycles and material property set 2 (visco thermo elasto–plastic with viscosity at low temperature).

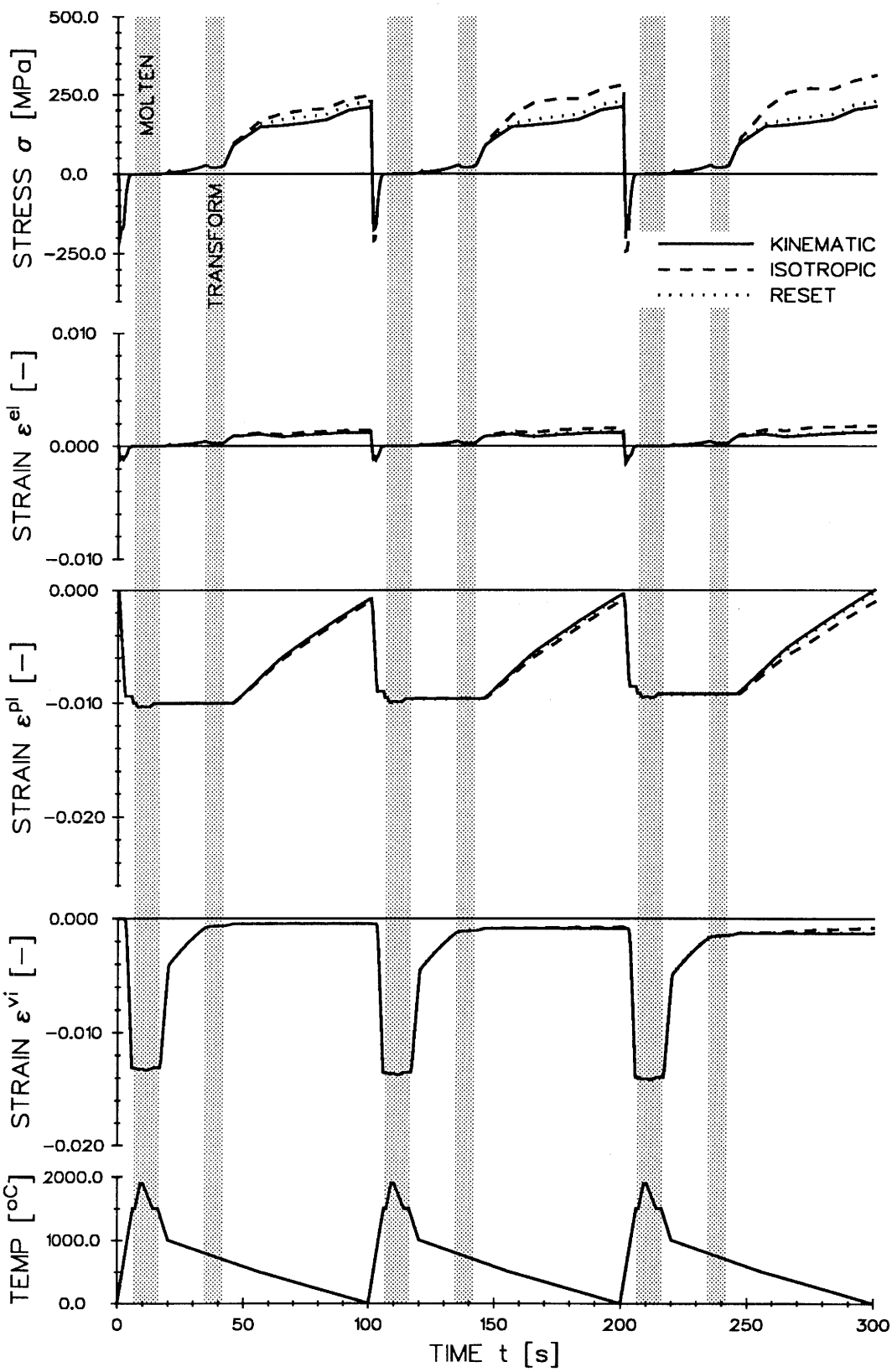

Fig. 2.15: Evolution of stress and strain for material property set 3 (visco thermo elastic–plastic with viscosity at high temperature).

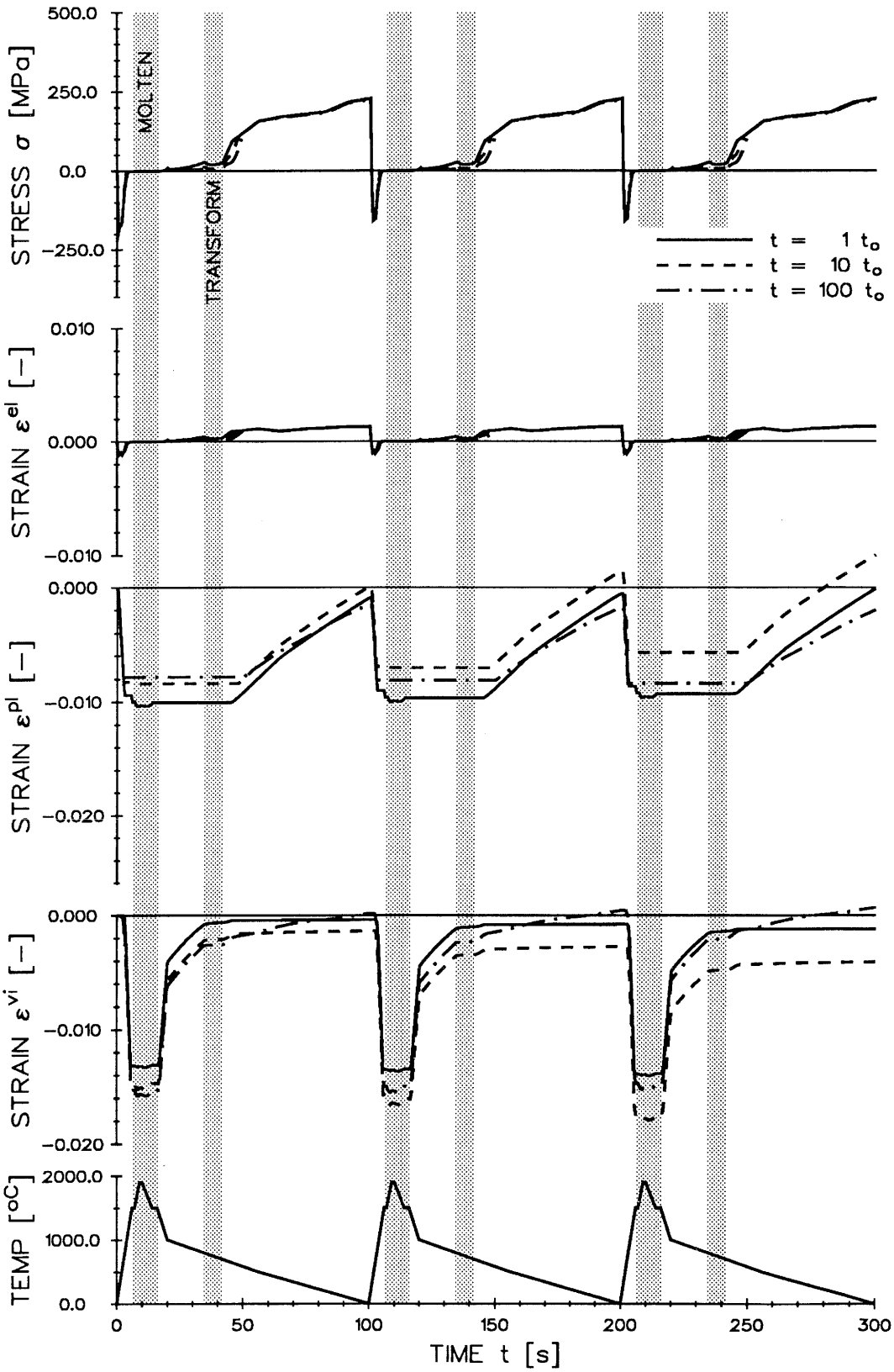

Fig. 2.16: Evolution of stress and strain for different loading periods of the temperature cycles and material property set 2 (visco thermo elasto–plastic with viscosity at low temperature).

2.4 Procedure for the finite element calculation in simulating a welding process

A completely decoupled procedure is used for the thermomechanical calculation of the residual stresses due to welding using the finite element method (Table 14). In a first step, the evolution of the temperature fields during a welding process are determined with the help of a weld heat source model (ATTINGER 1987 and MEYER & ATTINGER 1987). Temperature transients from these calculations serve as a loading in the mechanical calculation. One assumes thereby that heat generated by mechanical processes (e.g. plastic deformation) can be neglected compared to the heat input from welding and, further, that the deformations will be small enough to allow the temperatures in the undeformed state, i.e. for the initial geometry, to be calculated.

The thermomechanical calculations need more computation time than the temperature calculations. Therefore, the stresses, strains and deformations are determined at selected times with larger time increments to avoid excessively time–consuming calculations. However, this need contradicts the requirement for small time increments for accurate results. A good compromise seems to be found when time increments are chosen which have to produce maximum temperature increments of about 50 °C. The choice of the length of time increments is restricted in the thermomechanical finite element code SOLVIA. Therefore, they are incorporated into the proposed (and in the following discussed) material model by a table which is specific for the problem considered.

The severe loading condition of rapid heating and cooling in combination with a steep drop in yield strength at high temperatures poses problems. The finite element codes were not able to circumvent these problems in the days when the work was started, whereas today's upgraded version of ADINA has already implemented an improved algorithm to solve this kind of problem. To overcome them, a user–supplied material model was proposed for the finite element code SOLVIA in which one calculates the stress–strain relation for the integration points on the basis of isotropic, thermo elasto–plastic material behaviour, considering a von Mises yield criterion and isotropic hardening. The proposed material model incorporates in the main the commonly used so–called 'radial return' method (WILKINS 1964); the non–admissible stresses outside the yield surface obtained by the stress increment are forced back to the yield surface radially in the deviatoric stress plane (Fig. 2.17).

Table 14: Decoupled procedure to simulate a welding process.

Weld heat source	
Localized intense heat input ↓ Heat flux	Heat distribution
Temperature distribution (finite element method)	
Heat flux ↓ Temperature transients	Thermal conductivity Specific heat capacity Latent heat effects Convective and radiative heat losses
Mechanical response (finite element method)	
Temperature transients ↓ Stresses, strains, deformations	Visco elasto–plastic material behaviour Temperature dependency of material properties Flow rule, hardening

Radial return method:

$$\sigma_{ij}^{new} = \delta_{ij} \cdot s^{hyd} + \rho \cdot s_{ij}$$

where:

δ_{ij}				Kronecker symbol
s^{hyd}	$= \frac{1}{3} \cdot \sigma_{kk}$			hydrostatic stress
s_{ij}	$= \sigma_{ij} - \delta_{ij} \cdot s^{hyd}$			deviatoric stresses
ρ	$= Rp_{0.2}/\sigma^{eff}$	for	$Rp_{0.2} < \sigma^{eff}$	ratio of radial return
	$= 1.0$	for	$Rp_{0.2} \geq \sigma^{eff}$	
$Rp_{0.2}$				current yield limit
σ^{eff}	$= \sqrt{\frac{3}{2} \cdot s_{ij} \cdot s_{ij}}$			effective stress

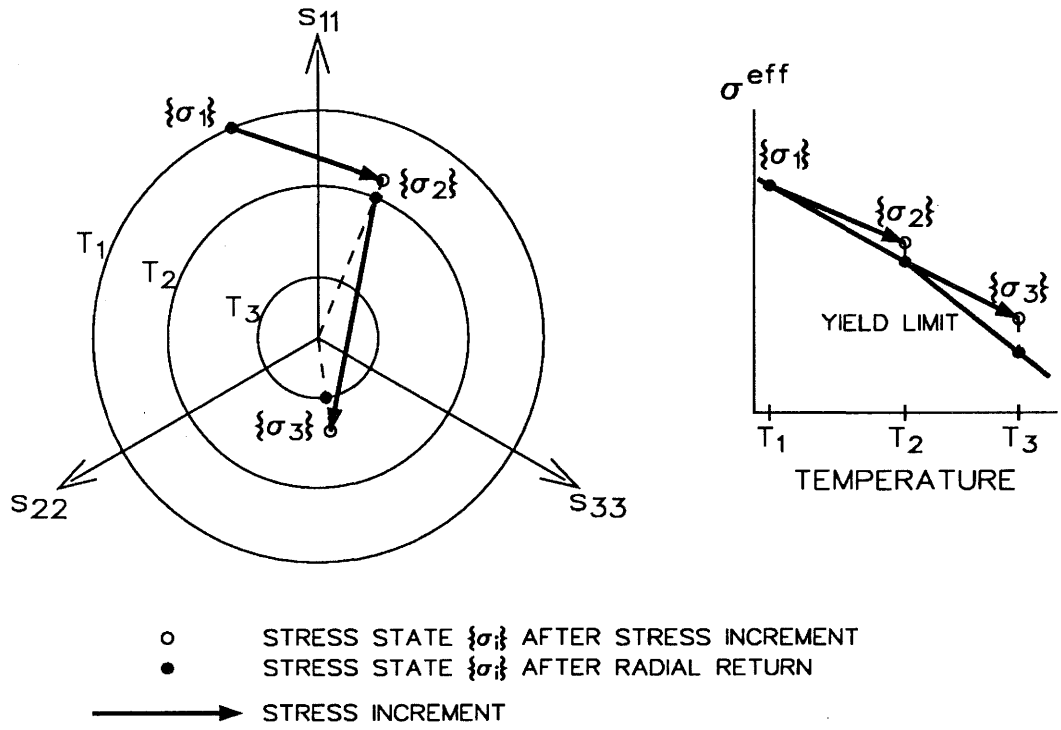

Fig. 2.17: Schematic presentation of the radial return method.

It is worthwile noting that the new stress state lies exactly on the yield surface with the radial return method thus eliminating the need for further iterations. The radial return method is simpler and more robust than the classical flow theory and sometimes produces different results. The constitutive models based on the flow theory being themselves an approximation to real material behaviour, it is difficult to establish whether the radial return method or the flow theory is better.

It was shown (ATTINGER et al. 1989) that the implementation of the radial return method in the proposed material model has a small influence on the evolution of the stresses and that it is important to correct the elastic strains and the plastic strains according to the stress drop effectuated in the radial return procedure,

$$d\varepsilon_{ij}^{el} = -(1.0 - \rho) \cdot s_{ij} / (2\mu)$$

$$d\varepsilon_{ij}^{pl} = +(1.0 - \rho) \cdot s_{ij} / (2\mu)$$

where: $d\varepsilon_{ij}^{el}$ change in elastic strains

$d\varepsilon_{ij}^{pl}$ change in plastic strains

μ Lamés shear constant

Creep strains are evaluated from a three–dimensional generalization of the uniaxial Norton's creep law. The consideration of viscous effects introduces a further set of problems into the thermo elasto–plastic calculation. Viscous strains are difficult to iterate when they become large compared to the elastic

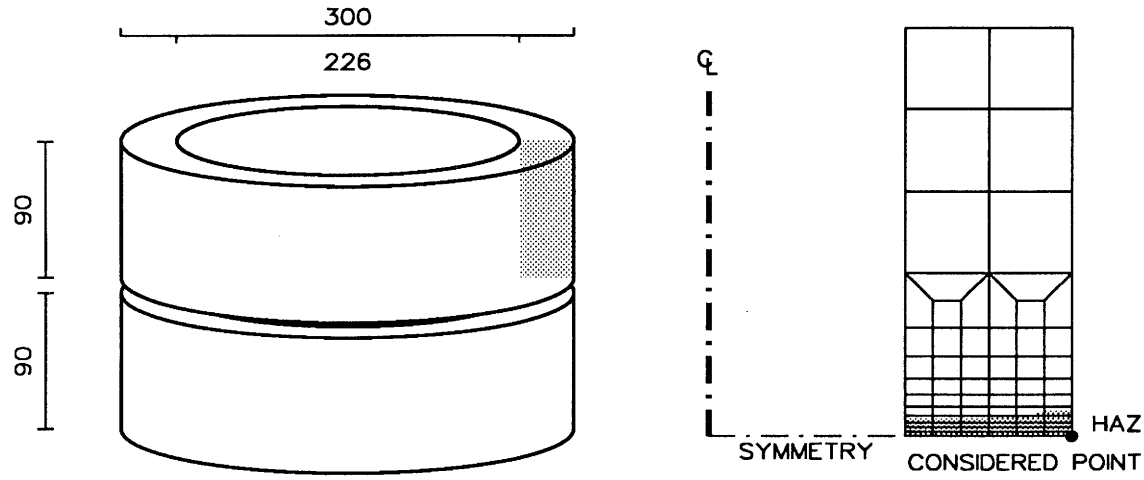

Fig. 2.18: The two annuli which are welded together by means of an electro–beam and the finite element mesh used in the calculations, together with the extension of the heat affected zone (HAZ).

strains. To circumvent this, a 'regula falsi' method was implemented into the material model, similar to the method that has been described for the FIBRE programme (Fig. 2.8).

Different methods are known to simulate molten material by a solid, an easy way to implement it in a running calculation without modifications of the code:

- Use of 64–bit computers which can handle large flexibility and low strength without problems.
- Finite elements with temperatures above the melting temperature are set inactive at liquefaction and are reset active at solidification.
- Temperatures above a certain cut–off temperature are reset to this temperature.
- Thermal expansion above the melting temperature is prevented by setting the coefficient of thermal expansion to zero.

The influence of these methods on the evolution of stresses and strains is discussed in the next paragraph. In addition, the chosen example taken from the literature should help to verify the proposed material model.

2.5 Verification of the proposed material model

Two annuli made out of a steel different to GS-40 are welded together (Fig. 2.18a) by means of an electro–beam which is described by MELANDER (1987). Melander performed his thermomechanical calculation with the finite element code ABAQUS on an axisymmetric mesh modelling one annulus (Fig. 2.18b). He used a thermo elasto–plastic material model, where the material properties are taken as temperature–dependent (Fig. 2.19). The

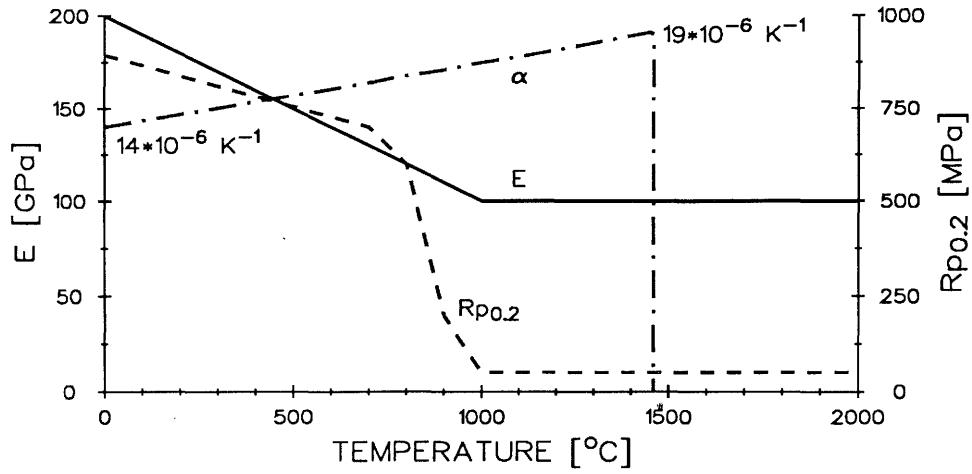

Fig. 2.19: Material properties used in the verification example (MELANDER 1987): modulus of elasticity E, yield limit $Rp_{0.2}$ and coefficient of thermal expansion α.

strength above1100 °C was assumed to be 50 MPa; this temperature range includes the solid and the molten material state. The Poisson ratio was kept constant (ν = 0.3), ideal plasticity (i.e. without hardening) was assumed and the coefficient of thermal expansion was set to zero for temperatures above the melting point. No further assumptions were introduced into the ABAQUS code to simulate the molten material state.

Temperature as a function of time and place from the calculation of the temperature field by MELANDER (1987) serves as loading for the thermomechanical problem (Fig. 2.20c). The ABAQUS code adjusts the time increments automatically to give adequate stress increments. The heat affected zone is shown in Figure 2.18b and the effective stress as a function of time in Figure 2.20b for a point just under the arc; the displacements are unfortunately not given by Melander. In the heat–up phase the effective stress is increased due to the thermal expansion, which is constrained by the surrounding cooler steel until the effective stress approaches the yield limit. The further heating reduces the temperature dependent yield limit and therefore also the effective stress. A scattered, low–value effective stress is obtained with the ABAQUS code during the molten material state. The final cooling phase allows the yield limit to increase and the effective stress is able to follow this increase.

A fictitious timescale is used in the SOLVIA code where the time increments have been chosen to produce maximum temperature increments of about 50 °C. The strength of the molten material was assumed to be at a very low level of 1 MPa. 4 cases of different assumptions involved in the stress calculation with molten material are investigated with the proposed material model. The evolution of the stresses and the radial displacement is given in Figure 2.20b and Figure 2.20c respectively.

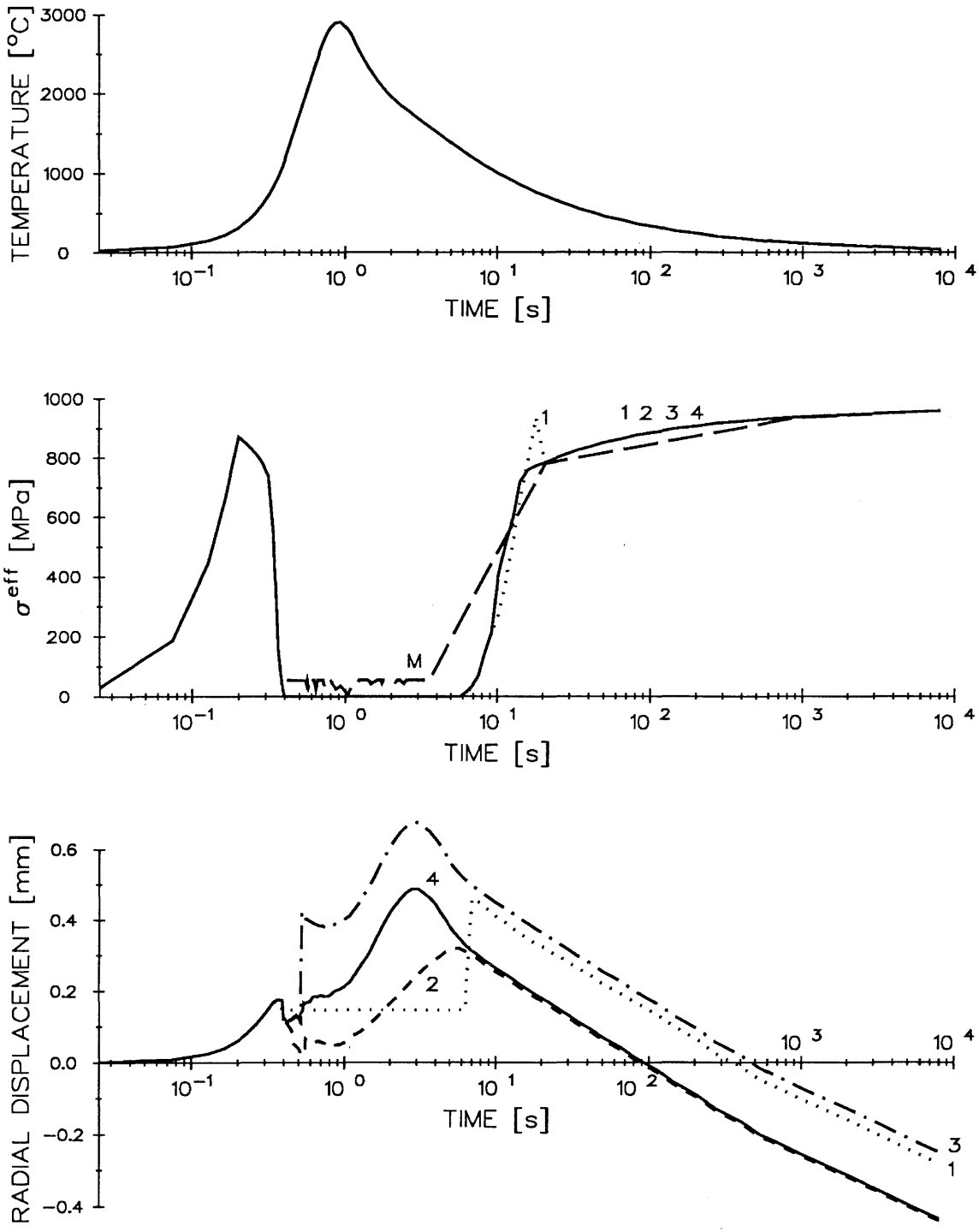

Fig. 2.20: Evolution of temperature, effective stress σ^{eff} and radial displacement in the verification example.

Case 1: Finite elements which have temperatures above the melting temperature are set inactive at liquefaction and are reset active at solidification. Since a whole element is set inactive/active because of a temperature at a single point, the transition temperatures are not sharply defined.

The liquefaction gives no problems. While the material is molten, the displacements are kept constant at a low effective stress. The solidification results in an abrupt and sometimes very large jump of the displacements and an increase of the effective stress with a later overshoot due to the inaccurately determined stresses at material transition. The final effective stresses match with those obtained by Melander.

Case 2: Temperatures above a certain cut–off temperature (1100 °C) are reset to this temperature, i.e. the material is kept solid at a temperature just below the melting temperature. Therefore, the final drop of the yield limit may be avoided in the heat–up phase, thus preventing possible numerical problems.

Small instabilities in the displacements are observed during the molten phase, whereas the displacements continue smoothly at liquefaction and solidification. The final effective stresses match with those obtained by Melander.

Case 3: The solidifying molten material is reset in a virgin state.

The liquefaction results in large changes of the displacements since no measures were taken to prevent instabilities. The solidification keeps the displacements and stresses smooth. The final effective stresses match with those obtained by Melander.

Case 4: The molten material is simulated by a solid with constant volume and no thermal expansion; it is further reset in a virgin state at solidification. Volume conservation was assumed to simulate the liquefied material more realistically. Melander proposed resetting the coefficient of thermal expansion to zero to eliminate further expansion; this procedure gives rise to large thermal strains at liquefaction and solidification and therefore to numerical problems. However, a smooth continuation without expansion is reached for temperatures above melting temperature if the coefficient of thermal expansion is chosen such that its product with temperature is constant, i.e. equal to the product at melting temperature.

Along the whole temperature cycle, the displacements develop rather smoothly and the effective stresses match with those obtained by Melander. The reset in a virgin state keeps the final plastic strains small (about 3 %), whereas the large strains obtained by Melander (about 28 %) are mainly produced during the molten material state.

Table 15: Assumptions used in the proposed material model to simulate molten material by a solid in the SOLVIA code.

Liquid phase simulated by a solid	The modulus of elasticity is kept at a rather high value for numerical reasons.
Volume conservation	The Poisson ratio is set to 0.5. A value of 0.48 will be used in the calculations for numerical reasons.
No thermal expansion	The coefficient of thermal expansion is chosen such that its product with temperature is constant, i.e. equal the product at melting temperature.
Small deviatoric stresses	The liquid without strength state is replaced by a low strength solid without hardening, thus maintaining the inability to sustain shear stresses.
No hydrostatic stress	The hydrostatic stress is set to zero for the molten material since welding produces a pool which is open to the surface and stress–free.
Virgin state at solidification	The past plastic strains, and therefore the past hardening, are reset to zero at solidification. The reference temperature for a stress–free state is assumed to be the melting temperature.
Rapid heating and cooling	The radial return method is implemented into the finite element code due to its inherent numerical problems for fast loading at high temperature.

The ABAQUS code showed no problems in calculating a welding process; the effective stresses sometimes fluctuate and no displacements were presented by Melander. The SOLVIA code needs some assumptions to circumvent the numerical problems involved in the welding process (Table 15). These assumptions are incorporated in a user–supplied material model where the liquid phase is simulated by a solid.

The verification example revealed that the assumptions used in the proposed material model have a negligible effect on the final effective stresses. The most evident parameter for judging the result turned out to be the displacement. The assumptions of case 4 including a low strength molten material (Table 15) will be used for further calculations due to the smooth transition of the displacements at liquefaction and solidification. Similar results to those with the assumptions of case 4 were obtained when temperatures above a certain cut–off temperature are reset to this temperature (case 2).

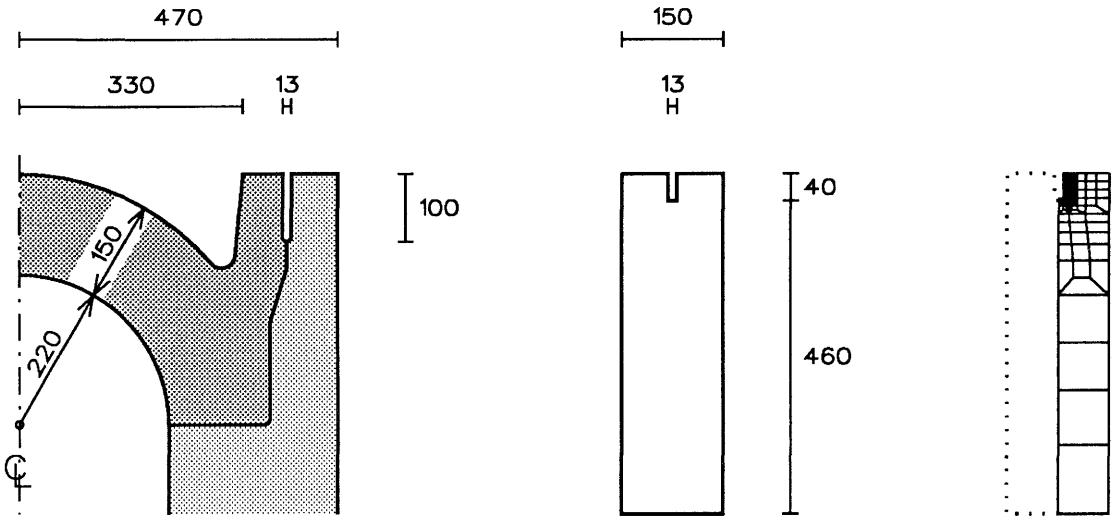

Fig. 2.21: The welding section of the overpack, its simplified two–dimensional, cubic model and the finite element mesh.

2.6 Residual stresses induced by multipass welding

The residual stresses due to multipass welding are determined using a simplified two–dimensional, cubic model of the overpack. The welding section of the overpack, its model and the finite element mesh used are depicted in Figure 2.21. The simulation model is 150 mm wide and 500 mm high and its depth is infinite. Thanks to symmetry, only one half of the workpiece has to be investigated and the bottom of the workpiece is fixed in the vertical direction. The workpiece includes a 13 mm wide and 40 mm deep groove. The groove is filled by submerged arc welding as is foreseen for the NAGRA reference overpack. The energy input rate is 10 kW and the welding speed (perpendicular to the cross section) 4.7 mm/s. A new layer of 4 mm thickness is deposited in each pass after 600 s.

The temperature transients were taken from the previous study (ATTINGER 1987). The peak temperatures computed pass by pass are given in Figure 2.22. The same size for the fusion zone (above 1480 °C) and the heat affected zone (above 750 °C) is obtained for the first 8 passes. The power density increases as the heat source reaches the surface. Therefore, a greater fusion and heat affected zone results at the top of the workpiece than below for a constant energy input rate.

A two–dimensional, plane strain thermomechanical calculation was performed, which considers material non–linearities only. The material behaviour is described by a multilinear thermo elasto–plastic, rate dependent material law according to the above–mentioned material model (Table 15). Isotropic hardening is assumed. The material properties for GS-40 cast steel at elevated temperatures are taken in the form of a table from the experiments as defined in the section 'material properties'. The weld material is assumed

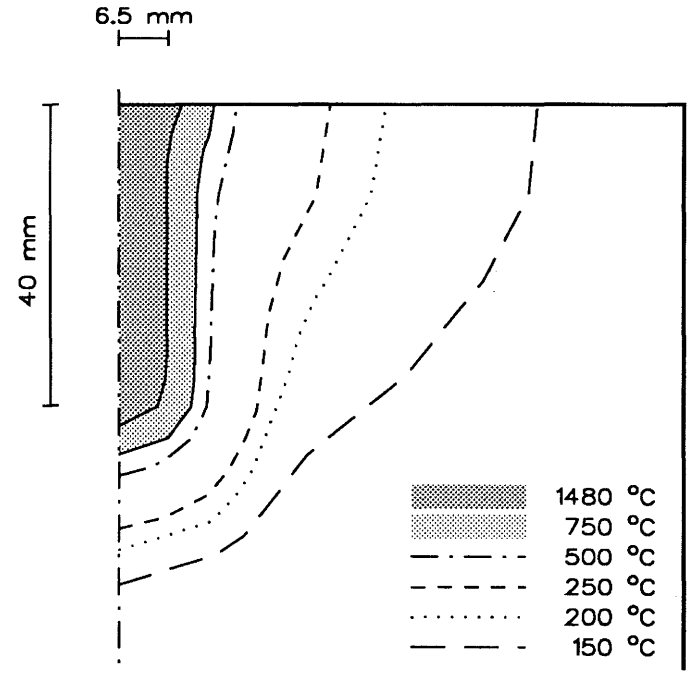

Fig. 2.22: Peak temperature in a 10 pass welding.

to behave like the parent material, the GS-40 cast steel. It was not attempted to determine the chemical composition of the solidified material in this work; the chemical composition of the material depends on the cooling rate and influences the material properties. The current values of the material properties are assumed to be constant over a time step.

The groove is simulated by inactive elements which are set active when they are deposited at the beginning of a pass; the deformed shape, and not the initial shape, is considered at the activation of these elements. The calculation cannot be performed beyond pass 8 due to the mesh being too deformed; remeshing would be necessary to overcome this problem.

The results at the end of a pass in the topmost 72 mm of the workpiece are shown in Figure 2.23 for a calculation with 8 weld passes performed pass by pass. The first pass produces large deformations in the bottom of the groove; further passes increase these deformations; their maximum value however maintains the position at about pass 3. The extension of plastic deformations is indicated by the dotted line in Figure 2.23. The largest effective plastic strain is produced in the edge of the groove at pass 1 and shifted to the centre on the same level of the workpiece in the later passes, thereby increasing its value asymptotically; the final value of 18 % is reached after pass 3. The highly strained zone is also extended; however, it no longer reaches the groove. The maximum tensile stresses were considered as the most relevant stress component concerning stress corrosion. The zone with tensile stresses matches with the zone of plastic deformations. The largest tensile stress (about 1000 MPa) is always about 8 mm below the groove.

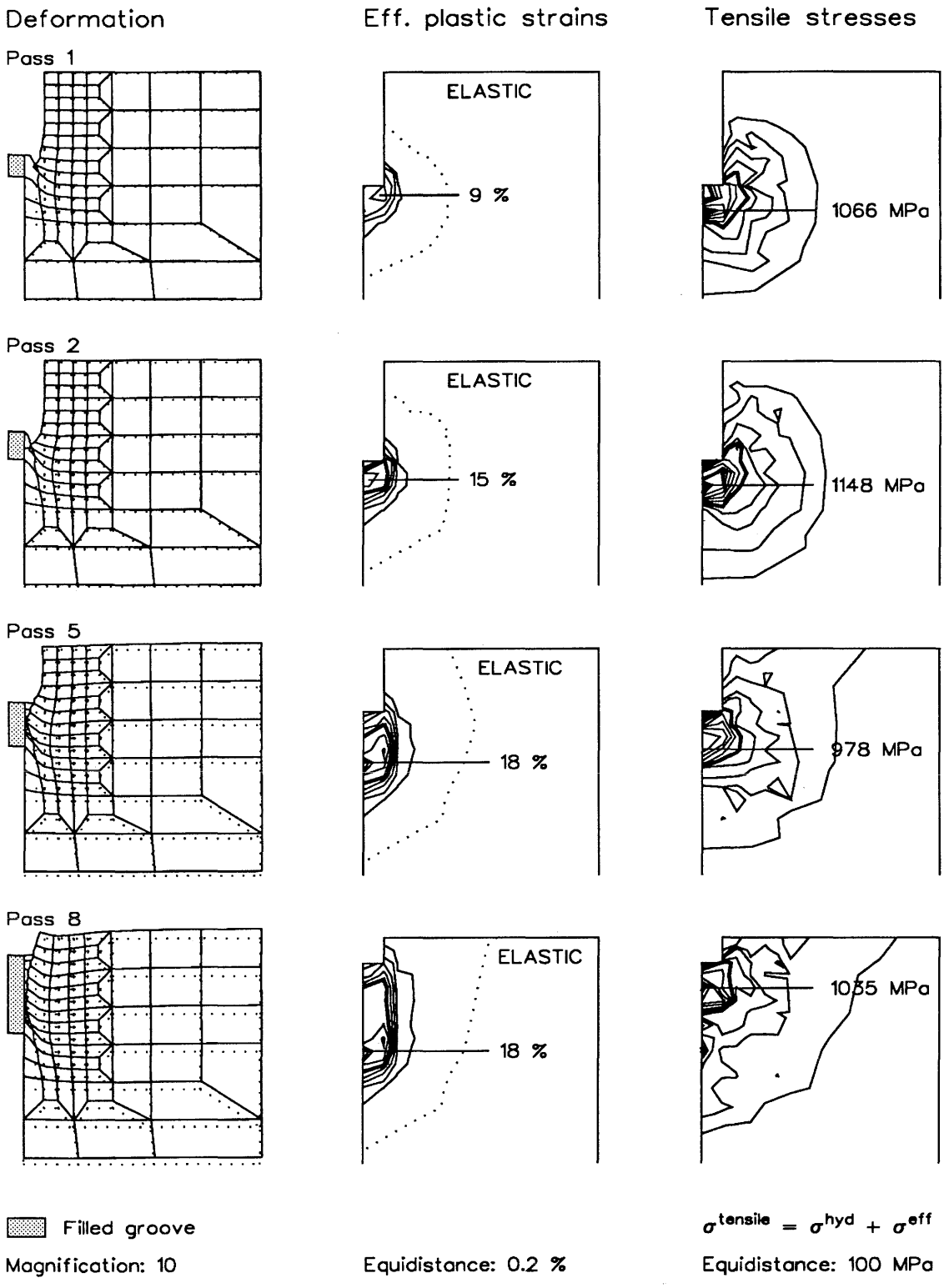

Fig. 2.23: Multipass welding with pass by pass calculation.

Tensile stresses of about 500 MPa prevail at the edge of the groove, a value which is similar to the yield limit at large strains. Figure 2.24 shows, in more detail, the evolution of the tensile stresses along the edges of the groove at the end of a welding pass. Scattered values are observed along the bottom, which are lower in the centre of the groove (around 180 MPa) than towards the corner (around 400 MPa). The maximum tensile stress along the wall is also found near to the corner. It decreases continuously during each welding pass, from about 570 MPa after pass 1 to about 270 MPa after pass 8.

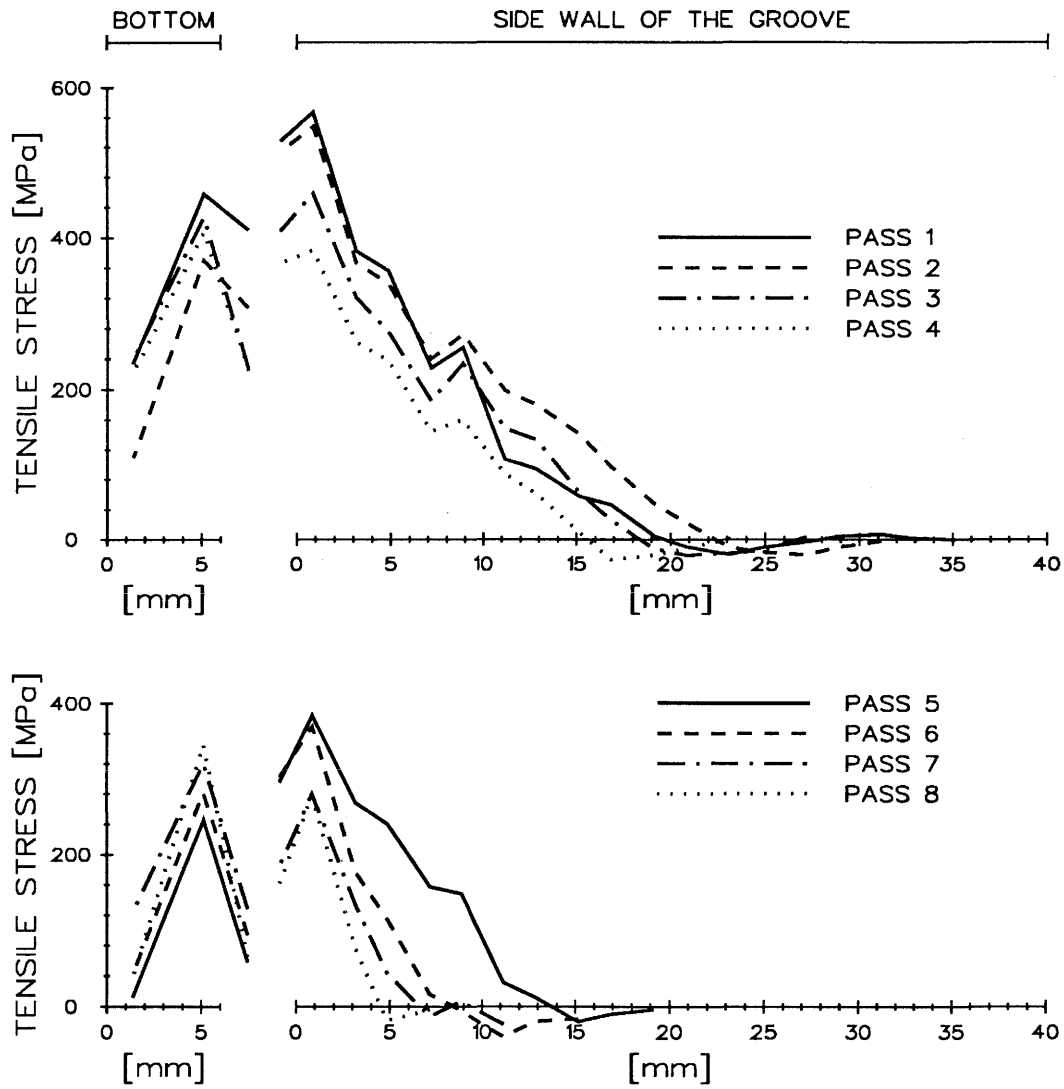

Fig. 2.24: Tensile stresses along the edge of the groove at the end of a welding pass. The position 0 mm indicates along the groove's bottom the centre of the groove and along the groove's side wall the bottom of the groove.

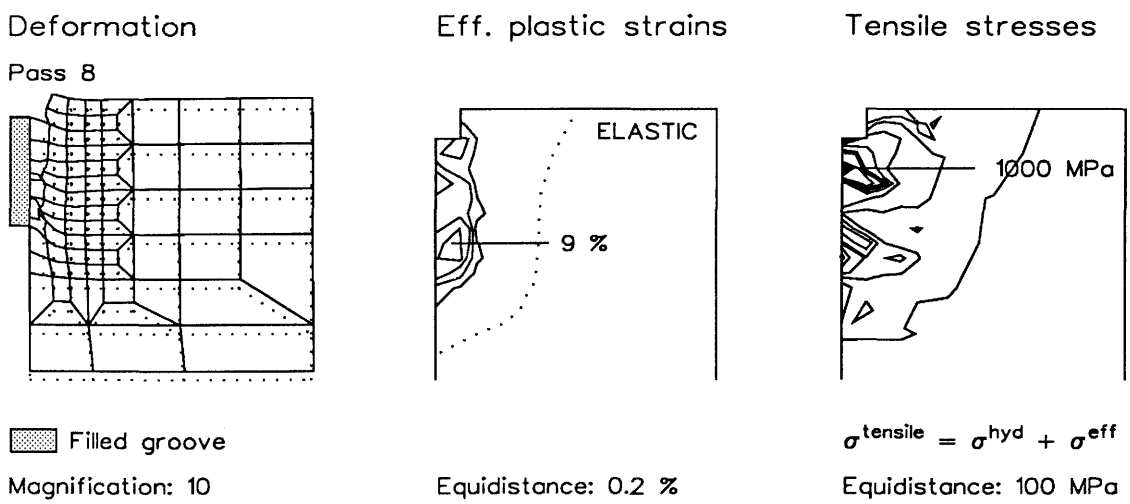

Fig. 2.25: Pass 8 of a multipass welding where only the passes 1, 4 and 8 are calculated.

A shorter procedure than the above very time consuming calculation of the residual stresses is tested in a calculation considering only the first, fourth and eighth pass. The results after the eighth pass are shown in Figure 2.25. The top of the workpiece is more deformed than in the pass by pass calculation whereas the displacements in the initial groove are smaller and unsteady, thus indicating that each pass acts independently. The strained zone has about the same extension, but at lower value than the pass by pass calculation. The stressed zones agree in their extension and in their value as well; only the stress peak still existing from the first pass is more extended in the shortened calculation.

2.7 Effect of cooling on stresses for heat-treated overpacks

The discussion so far has concentrated on stress build–up and relief in timescales of seconds to minutes. Therefore, viscous effects were neglected and, as a result, tensile stresses reached values in the range of the yield limit. However, viscous strains may become dominant over plastic strains at elevated temperature and when larger timescales are considered. It is assumed in the following that a filled and closed overpack is stress–relieved at 500 °C. The effect of viscosity on the residual stresses is studied during the cooling of this assumed stress–free overpack.

It is state–of–the–art that a post–weld heat treatment with a duration of several hours at a temperature between 600 °C and 650 °C would relieve most tensile stresses, provided the temperature is spatially constant over the whole overpack, especially during the cooling period. Even when economic aspects (size of furnace required) are neglected, heat treatment of the overpack in this temperature range would at first sight be ruled out because it would lead to an unacceptably high temperature in the waste (which itself

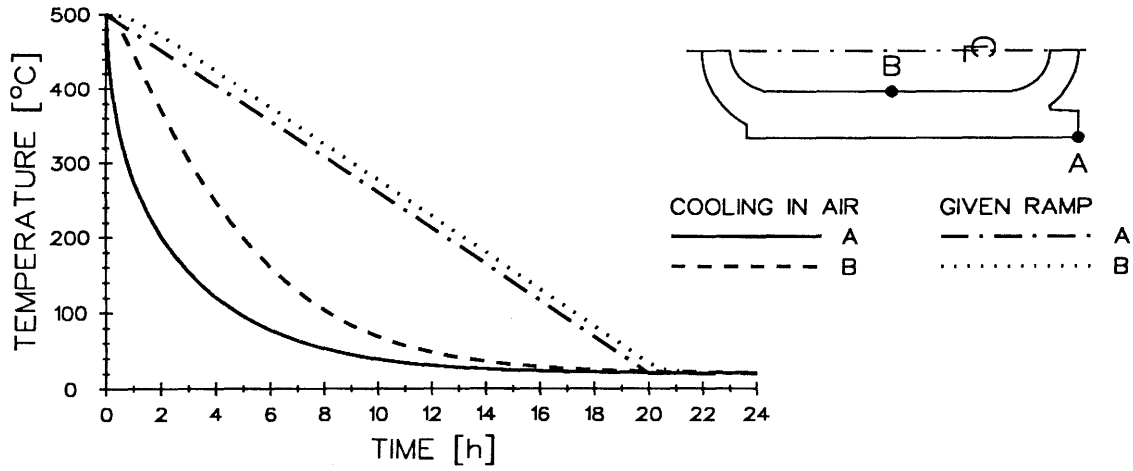

Fig. 2.26: Temperature evolution for the overpack in the cold spot A and the hot spot B for an overpack stress–relieved at 500 °C, with cooling in air as well as cooling with an assumed temperature ramp at the overpack's outside.

is generating radiogenic heat of order 0.5 kW per overpack) and thus to recrystallization effects in the borosilicate glass.

If, however, the issue is addressed in a more differentiated manner (in particular if the kinetics of the recrystallization process are considered), it appears that, at least in certain types of borosilicate glasses (GRAUER 1983), no recrystallization would take place for times of the order of 1 to 3 days at a temperature of 700 °C. If allowance is now made for a temperature difference of 150 °C between the hottest spot in the (heat–generating) waste and the outer surface of the overpack, then it is seen that a stress relief of the whole overpack at 550 °C may be acceptable.

Further modelling is performed with the aim of assessing whether the stress relief expected after such a heat treatment and its cooling to ambient temperature is sufficient to reduce the residual stresses due to welding. In this set of calculations, it is assumed that all stresses within the radioactive waste overpack are eliminated by annealing the filled and welded overpack at a temperature of 500 °C. This stress–free state serves as a starting point for the calculations in which the evolution of the stresses is studied during the cooling process. Two cases are considered: cooling in air and cooling with a given temperature ramp at the overpack's outside.

The temperatures are calculated with the finite element code ADINAT. A heat transfer coefficient steel–air of 0.050 W/mm^2 for the case with air cooling results in a cooling time for the overpack of approximately 18 hours (Fig. 2.26). Large temperature gradients (up to 180 °C after about 1.5 hours) between the cold spot A and the hot spot B suggest large stresses within the overpack. Therefore, a given temperature ramp at the overpack's outside was chosen to reduce them. The assumed temperature ramp decreases the temperature within 20 hours to ambient temperature (Fig. 2.26). A tempe-

rature gradient of about 20 °C results between the two spots A and B which is nearly constant over the whole of the cooling period.

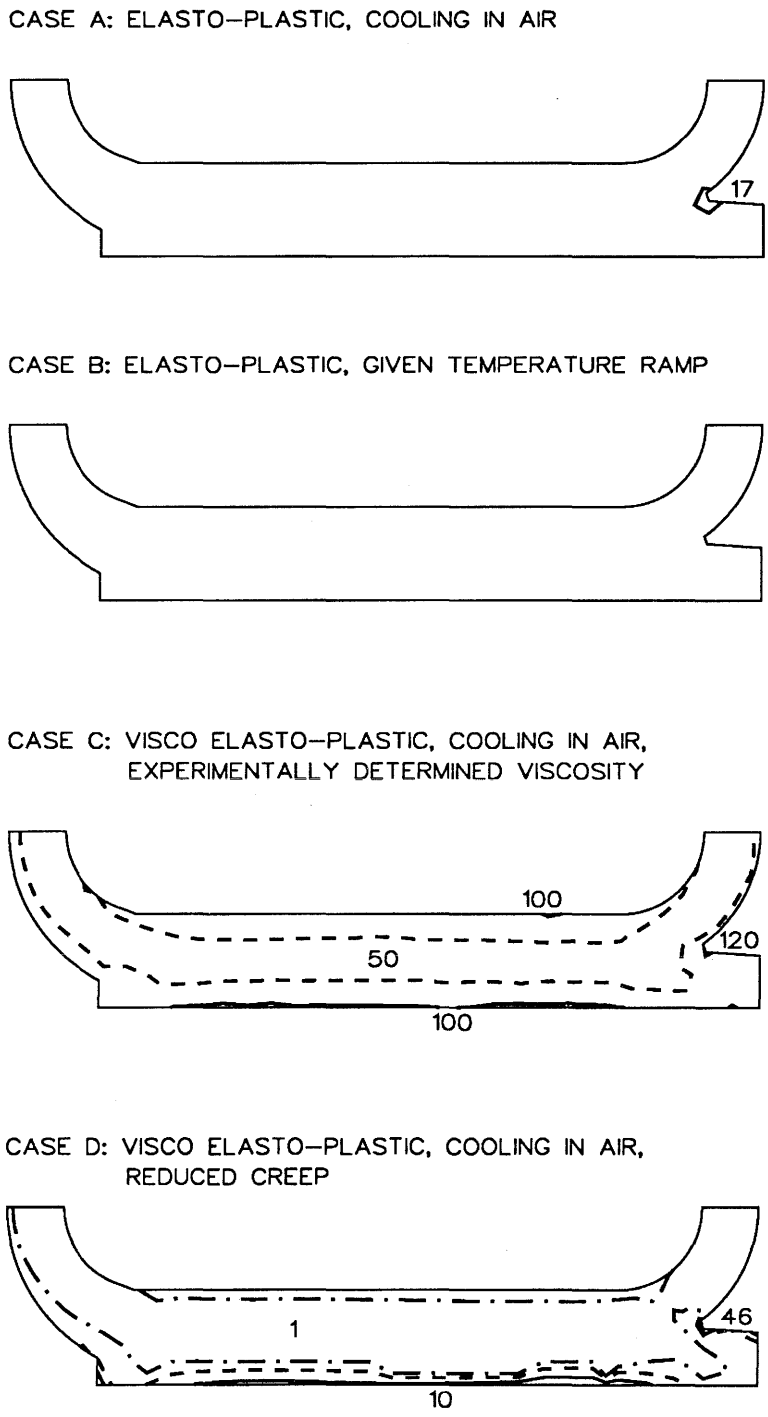

Fig. 2.27: Residual stresses at ambient temperature after the cooling of an overpack which was annealed at 500 °C to a stress–free state. The effective stresses σ^{eff} shown are in units of MPa.

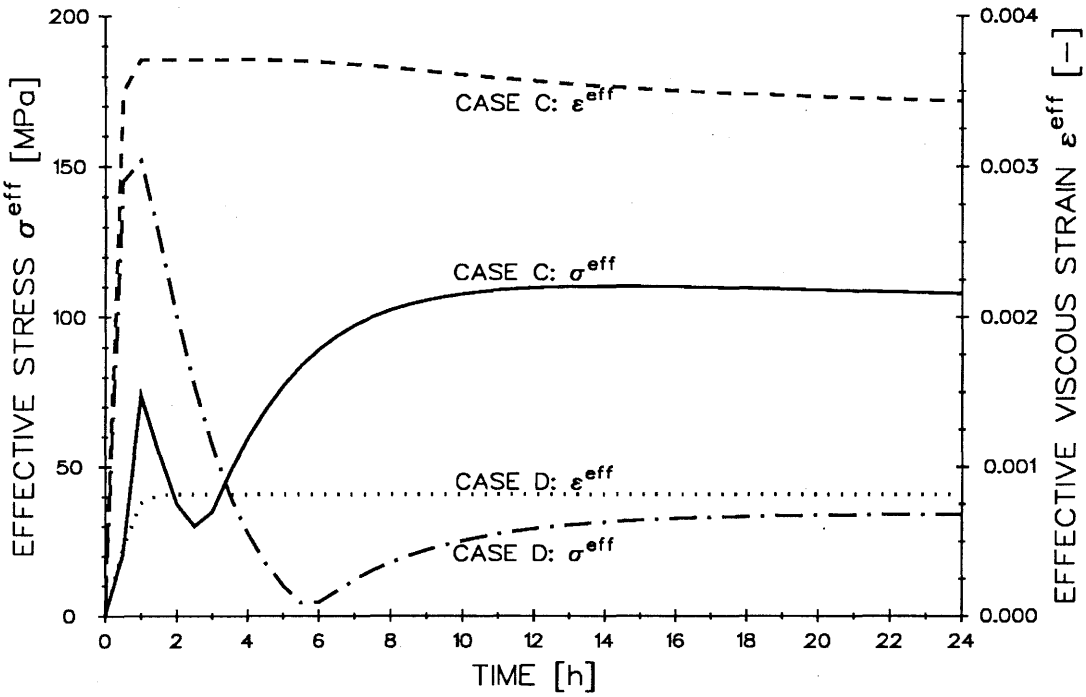

Fig. 2.28: Evolution of the effective stress and the effective viscous strain in the corner of the lid during cooling in air.

Temperature decrements of about 25 °C at the hot spot B and cooling in air were selected to determine the size of the time steps for the thermomechanical calculations. The same time steps were also used for cooling with the given temperature ramp.

First, an elasto–plastic material behaviour is assumed. Small residual stresses σ^{eff} remain in the body of the overpack after cooling in air despite the large temperature gradients during the cooling process. A small plastic zone is formed in the corner of the lid where residual stresses σ^{eff} up to 17 MPa prevail (Fig. 27a).

For the given temperature ramp, the temperature gradient is too small to produce any plastic zone and, therefore, no residual stresses are built up (Fig. 2.27b). One expects that the existing stresses during the cooling process may also be eliminated when the overpack is cooled down homogeneously. This behaviour was confirmed in a further (not presented here) calculation.

The case with cooling in air was studied in more detail, since it was hoped that its residual stresses would be further reduced when viscous effects are considered in the thermomechanical calculation. The two viscosity laws shown in Figure 2.9 were implemented in a visco elasto–plastic material model. The experimentally determined viscosity (number 2) produces residual stresses σ^{eff} of up to 120 MPa (Fig. 2.27c) and the viscosity, which is less at low temperature (number 3), produces residual stresses σ^{eff} of up to 46 MPa (Fig. 2.27d). The stress profiles generally follow the tempera-

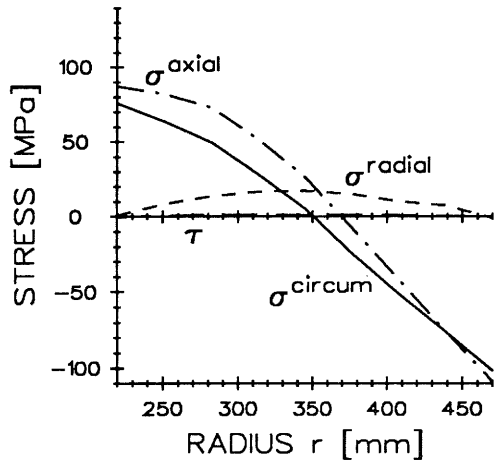

Fig. 2.29: Residual stresses along the radius at midheight of the overpack for cooling in air and considering the experimentally determined viscosity (Case C).

ture profiles. However, large stresses are also produced in the corner of the lid; they are much larger than those obtained with an elasto–plastic material behaviour.

The evolution of the effective stress and the effective viscous strain in the corner of the lid is depicted in Figure 2.28 to explain this unexpected behaviour. Viscous strains are produced in the first hour, i.e. for temperatures above 300 °C. The material is able to flow viscously in this temperature range. The amount of the viscous strain is proportional to the viscosity considered, the temperature level and the stresses which are given via the temperature gradient. These viscous strains are permanently locked in the overpack since reversed loading happens at a lower temperature level where the material is less able to flow. The onset of reversed loading is indicated in Figure 2.28 by the newly increasing effective stresses at around 4 hours.

It is a well known fact that a rapid cooling of a cylindrical body produces compressive residual stresses near the cooled surface and tensile stresses in its centre when an elasto-plastic material behaviour is assumed. As an exemple (Fig. 2.29), the residual stresses at midheigth of the overpack are discussed for the case C, i.e. for cooling in air and considering the experimentally determined viscosity. The circumferential stresses σ^{circum} and the axial stresses σ^{axial} are actually compressive at the outer surface and tensile at the inner surface. The axial stresses are due to the constraints by the hemispherical bottom and the hemispherical lid of the overpack. The radial stresses σ_{radial} are small, zero at the free surfaces and tensile in the interior. The shear stresses τ are very small indicating that the central part of the overpack's body can be considered as an axisymmetric problem.

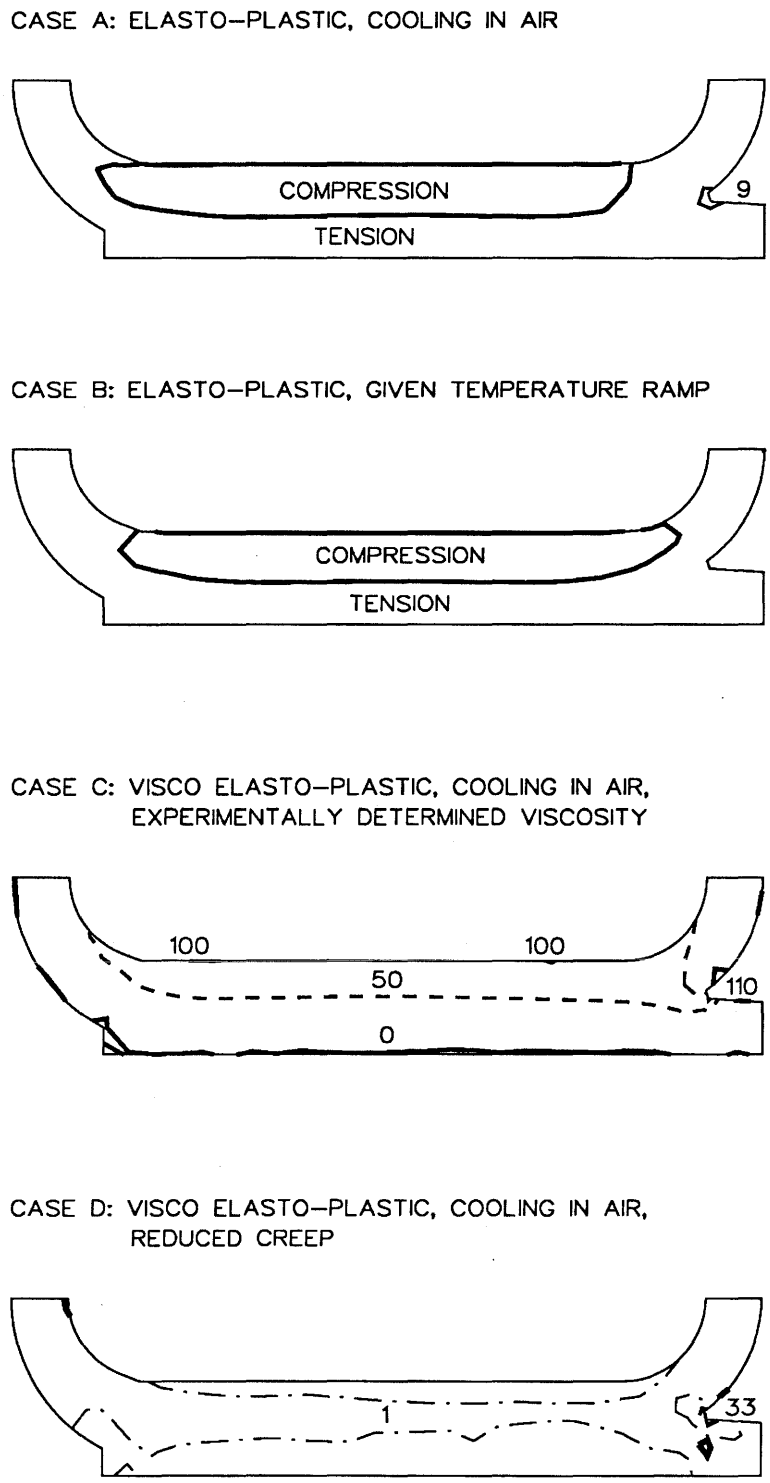

Fig. 2.30: Residual stresses at ambient temperature after the cooling of an overpack which was annealed at 500 °C to a stress–free state. The maximum principal stresses σ^{max} shown are in units of MPa.

The maximum principal stress σ^{max}, i.e. the envelope of the axial stress σ^{axial} and the radial stress σ_{radial} in the case C, would be tensile throughout the overpack. Figure 30 shows the maximum principal stresses σ^{max} which are considered to be the most relevant stress component concerning stress corrosion. At the surface, considerable tensile stresses are found in the corner of the lid where a small plastic zone was formed. Since the overpack's body was not plastified at midheight, the maximum principal stresses are small but compressive in the centre and tensile at the surface for an assumed elasto-plastic material behaviour. Case C results in a small layer along the surface which is compressed and in large stresses inside the overpack and at the lid.

It follows from these calculations on the cooling process after annealing that plastic strains can be prevented when viscosity is considered. However, this is only possible at the expense of newly generated permanent viscous strains. Therefore, the overall permanent strains may be smaller or larger for a visco elasto–plastic material behaviour than the plastic strains for an elasto–plastic material behaviour. As a consequence, it ruled out for a very viscous material and an inappriopriate cooling process that the yield limit will be reached again.

3 Summary

3.1 Modelling of overpacks under extreme loading conditions: the work performed within the COMPAS project

The COMPAS project allowed to develop a much better understanding of the modelling on how overpacks may respond to extreme pressure loadings.

- The benchmark exercises revealed the following features:
  - Non–axisymmetric modes of deformation may arise above a critical pressure in uniformly loaded profiles of uniform shape.
  - Plasticity is a factor that needs to be considered in fracture mechanics problems.
  - For a final creep state calculation, the treatment of viscous materials as a fluid turned out to be a feasible approach for studying the long–term creep performance.
- The preliminary testwork gave confidence in the general analytical capability. In general, good agreement was achieved in the preliminary testwork between experimental results and predictions for the cross–head displacement, but less good agreement for the crack mouth opening displacement in the rings with cracks. This probably reflects the lack of sophistication of many finite element codes in the area of fracturing.
- The experiments performed in the intermediate testwork demonstrated that the overpacks all failed by buckling in the mid–height region. The weld procedure used in the manufacture of the overpacks apparently had an effect on their overall strength, although this was very small. It was also concluded that localized reductions in wall thickness will not greatly reduce overpack failure pressure. The overall predictions were not as accurate as had been achieved in the simpler exercises of the preliminary testwork, reflecting the more complex nature of the problem.
- The partners' results for the advanced testwork demonstrated the benefit of the experience gained from the calculations of the intermediate testwork overpacks. Predictions of the behaviour of the axisymmetric overpack A1 were generally more accurate than the corresponding results in the previous phase, despite the overpacks now being of more complex geometry; results for the two non–axisymmetric overpacks were not good overall (OAP predicted failure pressure very accurately and PSI/NAGRA also gave a good prediction). Post–test examination of overpack A3 revealed no evidence of crack formation from the machined crack tip.

- The results from the COMPAS project have gone a long way towards giving confidence that finite element models can be used to predict the long-term behaviour of overpacks in the repositories. The performance of a computer code is dependent on the user and available computing power (demands on which became very excessive during the advanced testwork of the COMPAS project), as well as the technical abilities of the code itself.

- PSI/NAGRA demonstrated the ability to model the overpacks to a consistent level of accuracy with the finite element code ADINA. ADINA is a valuable analytical tool for such problems. It is suitable for calculations with elasto–plastic material behaviour and large displacements, for transient creep calculations and, in connection with the post–processor ORVIRT, for fracture mechanics calculations.

3.2 Study on some fundamental aspects of modelling stresses induced by welding

The parametric study with the one–dimensional FIBRE programme indicates the following features:

- Isotropic and kinematic hardening give the same results if the hardening is reset and full loading cycles with melting are considered.

- Mainly in the cooling phase and at high temperatures, plastic strains are suppressed at the expense of viscous strains. The heating rate in welding is so fast that it is hardly influenced by the viscosity. Viscous effects were observed at temperatures above about 500 °C for the material property set representative for GS-40 cast steel.

- The residual stresses are in the order of the yield limit at the final temperature for a thermo elasto–plastic material behaviour. Viscosity can reduce these residual stresses since it may prevent the evolution of plastic strains and thereby reduce the hardening.

3.3 Verification of the proposed material model

- The welding process poses different problems for a thermomechanical calculation with finite element codes: (1) the severe loading condition of rapid heating and cooling in combination with a steep drop in yield strength at high temperature, (2) viscous strains are difficult to iterate when they become large compared to the elastic strains and (3) the simulation of the molten material. A user–supplied material model is proposed to circumvent these problems.

- The proposed user–supplied material model incorporates the so–called 'radial return' method. The molten material is simulated by a solid which considers no thermal expansion and volume conservation and where the stresses are set to zero and the material is reset in a virgin state at solidification.

- The proposed user–supplied material model was verified for an elasto–plastic material behaviour on annuli which were welded together by means of electro–beam welding.

3.4 Residual stresses induced by multipass welding

The residual stresses are determined for a mulltipass welding of the lid of the NAGRA reference overpack. A completely decoupled procedure is used for this thermomechanical calculation by the finite element method:

- The assumptions used in the thermomechanical calculations turn out to be important for the resulting shape of the workpiece; however, they are insignificant for the residual stress field since this is defined by the yield limit with time independent material behaviour.

- The calculated residual stresses obtained from multipass welding are high. The tensile stress component reaches values of up to about 400 MPa.

- The pass–by–pass calculation in a multipass welding may be shortened by analyzing only each n–th pass. It was shown for the tensile stresses that a calculation with each fourth pass gives good agreement with a pass–by–pass calculation.

3.5 Effect of cooling on stresses for heat-treated overpacks

It was assumed that all stresses within the overpack are relieved by annealing the filled and welded overpack at a temperature of 500 °C. The calculations of the cooling process from the annealing to the ambient temperature show:

- The stress–free state may be maintained if an appropriate cooling procedure is chosen.

- Too rapid cooling may produce plastic deformations and therefore also residual stresses. These residual stresses are limited by the yield point of the alloy.

- Plastic zones are not observed when a visco elasto–plastic material behaviour is considered instead of an elasto–plastic one. However, the large viscous strains obtained at temperatures above 300 °C are

frozen in during the progressive cooling process. These may produce tensile stresses in the range up to the yield limit.

- Tensile stresses are observed at the surface. They are considerable in the corner of the lid. They tend to become tensile at the outer surface of the overpack's body although the circumferential and the axial stress components are compressive.

Acknowledgements

This work was performed within the framework of NAGRA's working group 'Simulation of the welding process'. We greatly appreciate the valuable discussions with colleagues from this working group – Dr. B. Knecht (NAGRA, Wettingen), R. Meyer (SENAP, Zürich), Dr. A. Rosselet and Dr. J. Simpson (SULZER INNOTEC, Winterthur). We also thank Dr. I. Hagenlocher (NAGRA, Wettingen) for support in the final stage of this work.

The experimental work of the COMPAS project was performed under contract from the 'Commission of the European Communities' within the framework of the European Atomic Energy Communities' cost–sharing research programme on radioactive waste management and disposal. The experiment with two annuli welded together by means of electro–beam welding was due to Dr. M. Melander (ABB Research Centre, Dättwil/Baden). All these experiments were very valuable in verifying and validating the finite element code used.

We also thank our colleagues Dr. Ph. Tipping, Dr. R. Rösel and Dr. B. Tirbonod (LWR–Safety Research Program at the Paul Scherrer Institute, Würenlingen) for their reviewing of the paper.

References

ADINA 1984: ADINA – A Finite Element Program for Automatic Dynamic Incremental Nonlinear Analysis: User manual. ADINA Engineering Inc., Watertown (MA., U.S.A.).

ATTINGER, R. 1987: Temperature Field Due to Multipass Welding of Radioactive Waste Containers. SMiRT **9**, Vol. B, pp. 69-74.

ATTINGER, R., HEER, W., WYDLER, P., DESPREZ, D., LOUVET, J., ZUCCHINI, A. 1989: Thermal and Mechanical Behaviour of a Subassembly Hexcan Under Total Instantaneous Blockage Conditions; a Code Comparison. SMiRT **10** Vol. E, pp. 311-316.

ATTINGER, R., KNECHT, B., MERCIER, O., ROSSELET, A., SIMPSON, J.P. 1991: Residual Stresses and Stress Corrosion Effects in Cast Steel Nuclear Waste Overpacks. Nuclear Engineering and Design, **129**, pp. 89-99.

BASS, B.R., BRYSON, J.W. 1983: Applications of Energy Release Rate Techniques to Part–Through Cracks in Plates and Cylinders. Volume 2 – ORVIRT: A Finite Element Program for Energy Release Rate Calculations for 2–Dimensional and 3–Dimensional Crack Models. NUREG/CR–2997 Volume 2, Oak Ridge National Laboratory ORNL/TM–8527/V2.

GRAUER, R. 1983: Glasses Used in the Solidification of High Level Radioactive Waste: Their Behaviour in Aqueous Solutions. NAGRA technical report NTB 83–01 E, Baden (Switzerland).

MELANDER, M. 1987: Calculation of Stresses and Strains in Electro–Beam Welded Plates. Euromech 221: The Mechanical Effects of Welding, Luleå (Sweden), June 15–17
and personal communications.

MEYER, R., ATTINGER, R. 1987: Transiente Temperaturfelder bei Nahtschweissungen. NAGRA technical report NTB 87-06, Baden (Switzerland).

NAGRA Working Group on Container Technology 1984: An Assessment of the Corrosion Resistance of the High–Level Waste Containers Proposed by NAGRA. NAGRA technical report NTB 84–32, Baden (Switzerland).

OVE ARUP & PARTNERS 1989a: A Directory of Computer Codes Suitable for Stress Analysis of HLW Containers – COMPAS project. CEC report EUR 12052 EN, Office for Official Publications of the European Communities, Luxembourg.

OVE ARUP & PARTNERS 1989b: Stress Analysis of HLW Containers – COMPAS project. CEC report EUR 12053 EN, Office for Official Publications of the European Communities, Luxembourg.

OVE ARUP & PARTNERS 1989c: Stress Analysis of HLW Containers: Preliminary Ring Test Exercise – COMPAS project. CEC report EUR 12401 EN, Office for Official Publications of the European Communities, Luxembourg.

OVE ARUP & PARTNERS 1990a: Stress Analysis of HLW Containers: Intermediate Testwork – COMPAS project. CEC report EUR 12593 EN, Office for Official Publications of the European Communities, Luxembourg.

OVE ARUP & PARTNERS 1990b: Stress Analysis of HLW Containers: Advanced Testwork – COMPAS project. CEC report EUR 12702 EN, Office for Official Publications of the European Communities, Luxembourg.

RICHTER, F. 1973: Die wichtigsten Eigenschaften von 52 Eisenwerkstoffen. Stahleisen–Sonderberichte, Vol. 8.

ROSSELET, A. 1988: Ergebnisse der Zugversuche mit dem Stahl GS–40. SULZER Brothers Ltd., Winterthur (Switzerland).

ROSSELET, A. 1990: Ergebnisse der Kriechversuche mit dem Stahl GS–40. Test certificate Nr. 2051, SULZER Innotec, Winterthur (Switzerland).

SIMPSON, J.P. 1984: Experiments on Container Materials for Swiss High–Level Waste Disposal Projects – Part II. NAGRA technical report NTB 84–01, Baden (Switzerland).

SOLVIA 1987: SOLVIA–PRE 87: User manual. Report SE 87–1, SOLVIA Engineering AB, Västerås (Sweden).

STEAG Kernenergie GmbH, MOTOR–COLUMBUS Ingenieurunternehmung AG 1984: Behälter aus Stahlguss für die Endlagerung hochradioaktiver Abfälle. NAGRA technical report NTB 84–31, Baden (Switzerland).

WILKINS, M.L. 1964: Calculation of Elastic–Plastic Flow. Methods of Computational Physics, Vol. 3, Eds. B. Alder, S. Fernbach and M. Rotenberg, Academic Press, New York (USA).